2
3
4
5 **Observations of Shoaling Internal Wave Transformation Over a Gentle Slope in**
6 **the South China Sea**
7
8
9
10
11
12
13
14

16 Steven R. Ramp[1], Yiing Jang Yang[2], Ching-Sang Chiu[3], D. Benjamin Reeder[3], and
17 Frederick L. Bahr[4]

19
20
21
22
23
24
25

27 Last modified April 25, 2022
28 Submitted to: Nonlinear Processes in Geophysics

30
31
32
33
34
35
36

38 [1] {Soliton Ocean Services LLC, Falmouth, MA 02540}

39 [2] {Institute of Oceanography, National Taiwan University, Taipei, Taiwan}

40 [3] {Dept. of Oceanography, Naval Postgraduate School, Monterey, CA 93943}

41 [4] {Monterey Bay Aquarium Research Institute, Moss Landing, CA 95039}

42 Correspondence to: S. R. Ramp (sramp@solitonocean.com)

43

44 **Abstract**
45
46   Four oceanographic moorings were deployed across the South China Sea
47 continental slope near 21.85°N, 117.71°E, from May 30 to July 18, 2014 for the
48 purpose of observing high-frequency nonlinear internal waves (NLIWs) as they
49 shoaled across a rough, gently sloping bottom. Individual waves required just two
50 hours to traverse the array and could thus easily be tracked from mooring-to-
51 mooring. In general, the amplitude of the incoming NLIWs tracked the fortnightly
52 tidal envelope in the Luzon Strait, lagged by 48.5 hours, but were smaller than the
53 waves previously observed to the southwest near the Dongsha Plateau. The type a-
54 waves and b-waves were observed, with the b-waves always leading the a-waves by
55 6-8 hours. Most of the NLIWs were remotely generated, but a few of the b-waves
56 formed locally via convergence and breaking at the leading edge of the upslope-
57 propagating internal tide. Waves incident upon the moored array with amplitude
58 less than 50 m and energy less than 100 MJ m^{-1} propagated adiabatically upslope
59 with little change of form. Larger waves formed packets via wave dispersion. For
60 the larger waves, the kinetic energy flux decreased sharply upslope between 342 m
61 to 266 m while the potential energy flux increased slightly, causing an increasing
62 ratio of potential-to-kinetic energy as the waves shoaled. None of the waves met the
63 criteria for convective breaking. The results are in rough agreement with recent
64 theory and numerical simulations of shoaling waves.
65

66

67

1 Introduction

Considerable field work has now been dedicated to observing and understanding the very large amplitude, high-frequency nonlinear internal waves (NLIW) in the northeastern South China Sea (SCS). It has now been well established that the waves emerge from the internal tide which is generated by the flux of the barotropic tide across the two ridges in the Luzon Strait [Buijsman et al., 2010a, 2010b; Zhang et al., 2011]. Both tidal conversion and dissipation are high around the ridges [Alford et al., 2011], but adequate energy survives to escape the ridges and propagate WNW across the sea. As they do so, the internal tides steepen nonlinearly until eventually the NLIW are formed [Farmer et al., 2009; Li and Farmer, 2011; Alford et al., 2015; Chang et al., 2021a]. The longitude where this takes place depends on the details of the forcing and stratification but based on satellite imagery it is not until at least 120° 30'E, roughly 50 km west of the western (Heng-Chun) ridge [Jackson, 2009]. This longitude is hypothesized to be the minimum distance/time required for the internal tide to nonlinearly steepen and break, or perhaps the first point where tidal beams intersect the sea surface west of the western ridge. Once the NLIW have formed, they propagate WNW across the deep SCS basin with remarkably little change of form [Alford et al., 2010; Ramp et al., 2010]. Once the waves start to shoal on the continental slope however, roughly between 1000m to 150m depth, the changes become quite dramatic. Wave refraction due to the shallower depth and changing stratification tends to align the wave crests with the local topography. Incident NLIWs which were initially solitary may form packets via wave breaking or dispersion [Vlasenko and Hutter, 2002; Vlasenko and Stashchuk, 2007; Lamb and Warn-Varnas, 2015]. Some very large waves may split into two smaller waves [Small 2001a, 2001b; Ramp, 2004]. When the wave's orbital velocity exceeds the propagation speed, usually between 300m - 150m depth, the largest waves may break and form trapped cores that transport mass and nutrients onshore [Farmer et al., 2011; Lien et al., 2012, 2014; Rivera-Rosario et al., 2020; Chang et al., 2021b]. Still farther onshore where the upper layer thickness exceeds the lower, the depression waves are transformed into elevation waves [Orr and Mignerey, 2003; Duda et al., 2004; Ramp et al., 2004; Liu et al., 2004]. The elevation waves presumably continue propagating WNW towards shore and dissipate in shallow water, but observations to the west of this point are scarce.

Two types of NLIWs, called a-waves and b-waves, have been repeatedly observed, a parlance first coined by Ramp et al. [2004]. Based on the Asian Seas International Acoustics Experiment (ASIAEX) results, the a-waves consisted of rank-ordered packets that arrived at the same time every day and were generally larger than the b-waves, which were usually solitary and arrived one hour later each day. It has subsequently been shown via longer data sets that the timing is not universal, and that b-waves may sometimes be larger than a-waves [Alford et al., 2010; Ramp et al., 2010]. It is now recognized that the a-waves are generated in the southern portion of the Luzon Strait and the b-waves to the north [Du et al., 2008; Zhang et al., 2011; Ramp et al., 2019]. The b-waves are subject to massive dissipation over the shallow

113 northern portion of the western (Heng-Chun) ridge [Alford et al., 2011] but the a-
114 waves are not. The distinction matters because the energy and propagation
115 direction of the trans-basin waves incident on the continental slope determines how
116 they behave as they shoal. These differences are explored further in this paper.
117
118 The present study was motivated by the discovery of large (h > 15m, λ order 350m)
119 undersea sand dunes on the sea floor along a transect southeastward from 21.93°N,
120 117.53°E in the northeastern South China Sea [Reeder et al., 2011].   Subsequent
121 multi-beam echo surveys (MBES) during 2013 and 2014 revealed that the dunes
122 occupy at least the region spanning 21.8 to 21.9°N and 117.5 to 117.7°E (Figure 1).
123 This region is on the continental slope slightly northeast of the Dongsha Plateau.
124 The bottom slope in the dunes region is relatively slight with respect to steeper
125 bottom slopes progressing both offshore and onshore from the dune field. The sand
126 dunes are of interest due to their impact on shallow-water acoustic propagation,
127 and their interaction with shoaling internal tides and NLIWs traveling WNW up the
128 slope. The acoustic issues are addressed in other papers emerging from the
129 program [Chiu and Reeder, 2013; Chiu et al., 2015]. Oceanographic questions of
130 interest include: 1) How are NLIWs transformed as they shoal over a gentle slope
131 between 388m and 266m over the continental slope? 2) What are the physical
132 mechanisms responsible for this transformation? and 3) How does the increased
133 bottom roughness in the dune field affect energy dissipation in the shoaling internal
134 tides and NLIWs, relative to other locations? Geophysical problems of interest
135 include: 4) What, if any, is the role of the NLIW in sediment re-suspension and dune
136 building? 5) What determines the spatial scales of the dunes? and 6) Why are the
137 dunes located where they are, and why are they not observed elsewhere?
138
139 This paper addresses how the high-frequency nonlinear internal waves were
140 transformed under shoaling, while the NLIW dissipation and role in the dune-
141 building process will be addressed in separate works [Helfrich et al., 2022]. The
142 data and methods are described in section 2, the NLIW arrival patterns and their
143 relation to the source tides in section 3, and the wave transformations and energy
144 conservation in section 4. A summary and conclusion section follows.
145
146 **2 Data and Methods**
147
148 An array of four oceanographic moorings were deployed across the continental
149 slope from 21.81°N, 117.86°E (386 m) to 21.89°N, 117.56°E (266 m) during May 31
150 to June 18, 2014 (Figure 1, Appendix A). The moorings labeled YPO2, YPO1, CPO,
151 and RPO were separated by 4.10, 3.30, and 5.69 km respectively corresponding to
152 wave travel times of 36.5, 30.3, and 56 min between moorings. Temperature and
153 salinity were sampled at 60s intervals. Instrument spacing ranged from 15 m to a
154 maximum of 30 m in the vertical to resolve internal wave amplitudes. Currents at
155 RPO were sampled using three downward looking 300 kHz ADCPs moored at 27 m,
156 105 m, and 184 m depth which provided coverage of the entire water column except
157 the upper20 m. Currents at CPO were also sampled using three-300 kHz ADCPs, one
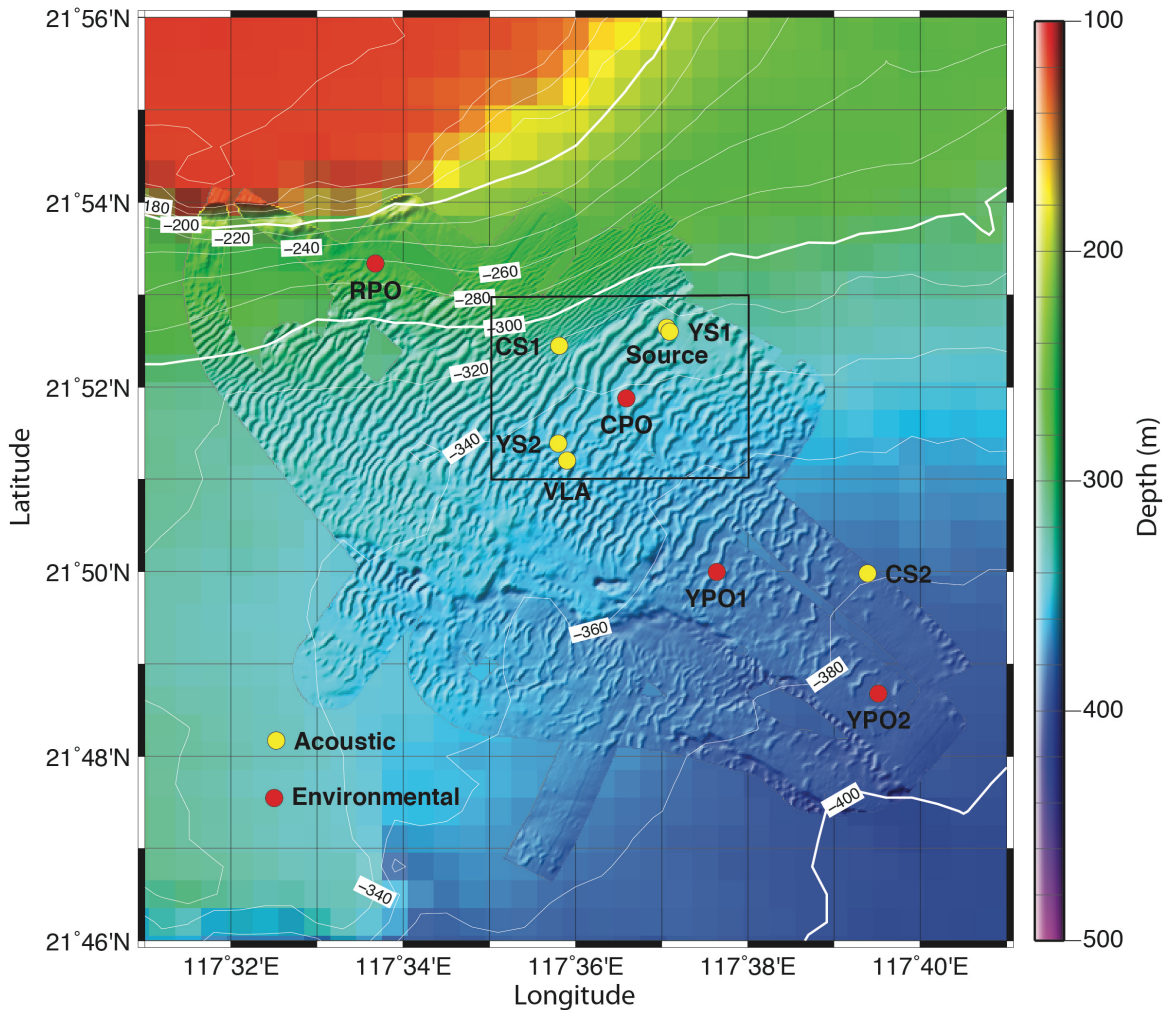
Figure 1. Locator map for the Sand Dunes 2014 field experiment. This paper primarily concerns the environmental moorings indicated by the red dots, although temperature from the "source" mooring is also used. The area within the black box is expanded in Figure 2.

downward-looking unit moored at 15 m depth, and an up/down pair at 264 m depth. Since the range of these instruments was nominally 100 m, there was an unsampled region spanning roughly 115 – 164 m depth at mooring CPO. Currents at YPO1 and YPO2 were sampled using one 75 kHz and one 300 kHz ADCP. The 75 kHz instruments were mounted downward looking in the top syntactic foam sphere at 20 m depth. The 300 kHz instruments were also mounted downward looking in cages at 300 m depth. The 300 kHz instruments burst-sampled for 20 s every 90 s, while the 75 kHz instruments sampled once per second and were averaged to 90 s intervals during post-processing. These sampling rates were adequate to observe the shoaling NLIWs with no aliasing. A fifth mooring labeled "source" on roughly the same isobath as CPO (Figure 1) sampled temperature only from 27 to 267 m.

176   This mooring was targeted for the same "trough" in the sand dune field as CPO to
177   examine along-crest acoustic propagation. It additionally proved useful to identify
178   the precise phasing and orientation of the internal wave crests in the along-slope
179   direction.
180
181   **3 Results**
182
183   *3.1 The Nature of the Dunes*
184
185   The stage is set by a zoomed-in view of the study region showing the seafloor sand
186   dunes as depicted by the MBES data (Figure 2). A change in the bottom slope forms
187   a very clear line of demarcation between lower (4 m) dunes with shorter (100 m)
188   wavelength and the larger (10-15 m) dunes with longer (260 m) wavelength. Dunes
189   in these regions were nearly sinusoidal. Farther down the slope in water > 360m
190   depth, the dunes were "parted" meaning the trough widths were much greater than
191   the crest widths. Mooring RPO was located in the first region with steeper slope,
192   CPO was in the second region of smaller slope and large sinusoidal dunes, and
193   moorings YPO1 and YPO2 were in a region with similar mean bottom slope but
194   parted dunes. Repeat MBES surveys indicated that during 2013-14, the dunes were
195   stationary to within the accuracy of the surveys. For purposes of this paper, the
196   most important fact about the bottom is the sharp, clear change of bottom slope
197   across the white dotted line (Figure 2) from 1:35 =.03 = 3% = 2.0° over the
198   shallower part to 1:160 = .006 = 0.6% = 0.3° over the deeper part. These slopes are
199   essential for comparing the observations to theory.
200
201
202
203   *3.2 Wave Arrival Patterns*
204
205   While fine-tuning the NLIW generation problem is beyond the scope of this paper, the
206   fundamental properties of the wave arrival patterns can be understood via comparisons
207   with the generating tide in the Luzon Strait. Having no remote observations during
208   spring 2014, the wave arrival patterns at the sand dunes moored array were compared
209   with the barotropic tidal forcing in the Luzon Strait as obtained from the TPXO7.0 global
210   tidal model [Egbert and Erofeeva, 2002]. The model output has been shown to be in
211   good agreement with the limited observations available in the Luzon Strait [Ramp et al.,
212   2010] and is thus a good indication of the tidal amplitude and phase at generation.
213
214   To begin, all the NLIWs arriving at the moored array were identified using large-scale
215   plots of temperature, salinity, and velocity. The arrivals were then summarized for the
216   entire time series by labeling the displacement of the 20°C isotherm from its mean
217   position at mooring RPO (Figure 3, top). The wave arrivals, as indicated by sharp
218   downward displacements of the isotherm, fall into two groups or "clusters" of waves each
219   within a fortnightly envelope. The waves were labeled using previous conventions, using
220   lowercase a- and b- for the first cluster and uppercase A- and B- for the second for
221   uniqueness. This nomenclature will be used to refer to individual waves subsequently.

222
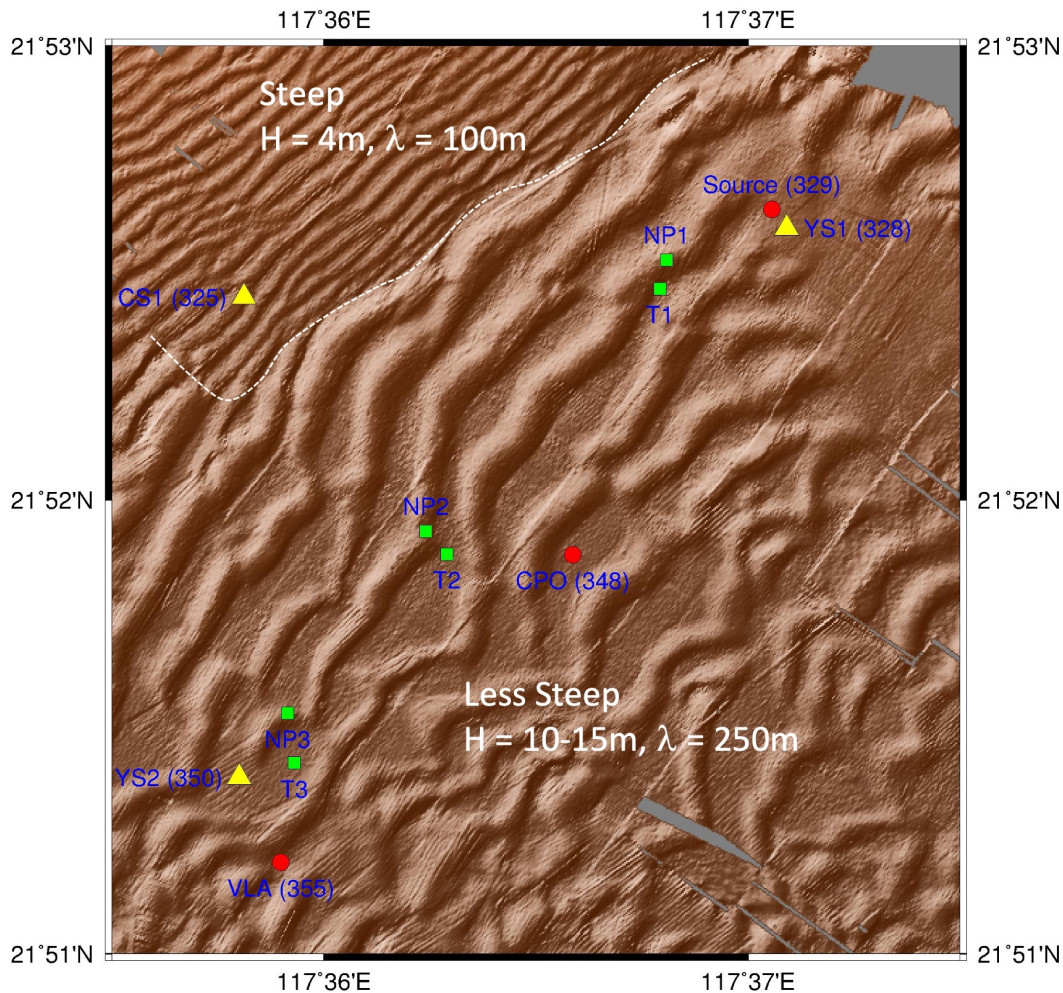
223
224
225
226 *Figure 2. The sea floor in the study region as observed by a multi-beam echo sounder*
227 *(MBES) survey during June 2014. The region is delineated by the black box in Figure 1.*
228 *The dotted white line indicates a sharp change in bottom slope, steeper towards the*
229 *northwest.*
230

231 There is no dynamical difference implied by the upper- vs. lowercase names. A total of
232 21 NLIWs with amplitude greater than 20 m were observed, 13 a-waves and 8 b-waves.
233 When b-waves were present, the waves arrived in b- and a- pairs with the b-wave always
234 leading the a-wave by on average 6.6 hours. The a-waves began arriving earlier in the
235 fortnightly cycle for instance 6/7 to 6/11. The b-waves began arriving later and grew
236 larger later in the fortnightly cycle. With the exception of 6/3 and 6/15, the a-waves were
237 larger than the b-waves.
238

239 The RPO wave amplitude time series was then plotted over the Luzon Strait tides (Figure
240 3, bottom) with the wave amplitudes lagged back by the propagation time from the
241
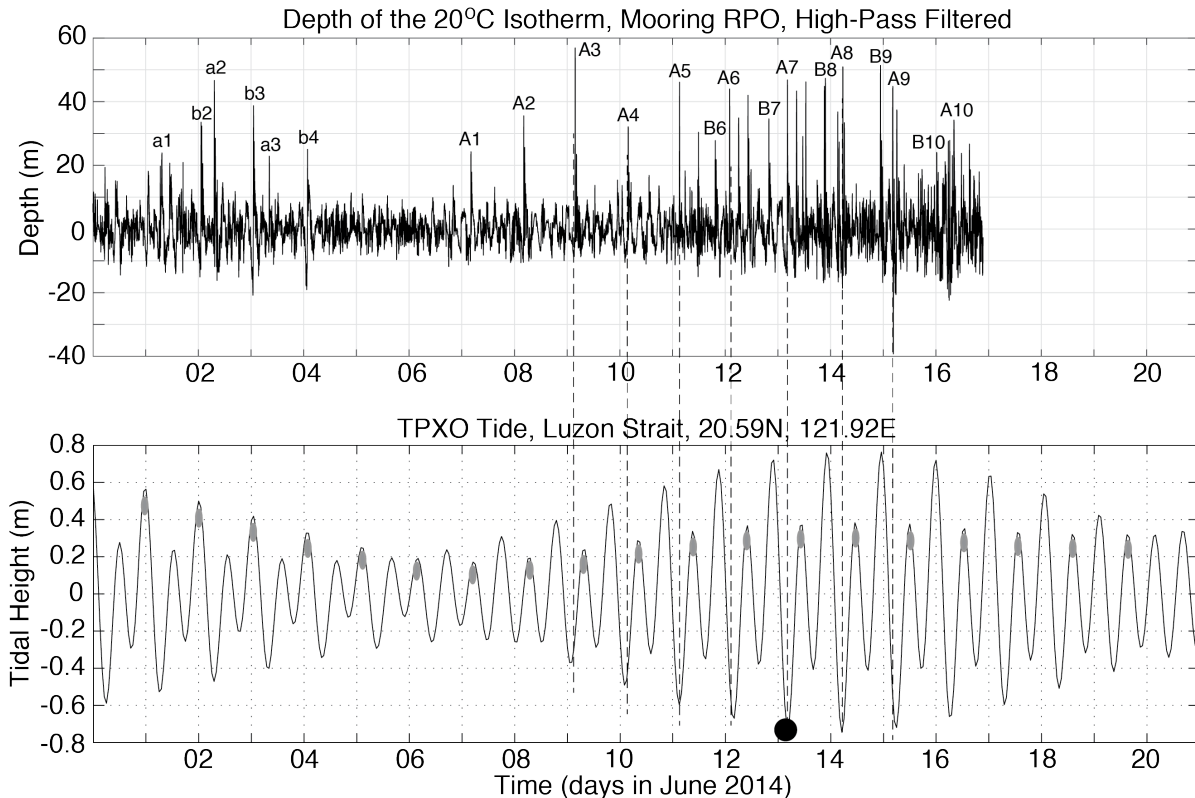
Figure 3. (Top) Time series showing the depth of the 20°C isotherm observed by mooring RPO located at the 266 m isobath (Figure 1). The time series was high pass filtered to separate thermal displacements due to NLIWs from the internal tides and mean (mesoscale and seasonal) flows. The sharp depressions of the isotherm indicate passing NLIWs. The type-a and type-b waves are labeled using lower case for the first fortnight and upper case for the second. (Bottom) Tidal amplitude in the central Luzon Strait from the TPXO global tidal model [Egbert and Erofeeva, 2002], at a point located between Batan and Itbayat Island in the Luzon Strait. The gray ellipses indicate how the major and minor tidal beats switched positions during the neap tide. The black circle indicates the time of the full moon on June 13th. The waves (top panel) have been lagged back by the propagation time from the strait (48.5 hours) to better align with the barotropic tidal envelope in the generating region. The vertical dashed lines show how the lagged a-waves aligned with the ebb tide in the straits.

source to the mooring. The lag time (48.5 hours) was estimated by making a small adjustment to the propagation time nearby (50.3 hours) which was calculated using a full year's data [Ramp et al., 2010]. Several obvious results emerge from this comparison. First, the NLIW amplitudes at RPO track the fortnightly tidal amplitudes in the Luzon Strait. The largest waves were generated at spring tide in the strait and no waves at all were generated during neap. This result is consistent with longer (11 month) time series obtained over the continental slope to the southwest [Chang et al., 2021a]. Second, the

267 generating tide was mixed, diurnal dominant, with a strong diurnal variation, but only the
268 major beats resulted in NLIWs in the far field. The minor beats and the neap tides were
269 apparently too weak to spawn NLIWs downstream. As a result, just one wave of each
270 type was generated per day, despite the generating tide being semidiurnal. The major and
271 minor beats switched positions during the neap tide, and the wave arrivals at the sand
272 dunes array switched positions accordingly. Third, the lagged a-waves aligned precisely
273 with the major ebb (eastward) tide in the Luzon Strait, in agreement with previous work.
274 This suggests generation by the lee wave mechanism [Buijsman et al., 2010a]. Finally,
275 the b-waves were sometimes aligned well with the major flood tide preceding each a-
276 wave, but we now believe this to be coincidence: The directional histograms (not shown)
277 show the a-waves on average traveling along a path about 24 degrees more northward
278 (294°) than the b-waves (270°), consistent with the primary source for the a-waves being
279 located farther to the south along the Luzon ridge system. The b-waves lead because
280 their generation site was closer to our observation point on the Chinese continental slope.
281
282 One example of the daily moored temperature time series at mooring RPO is shown to
283 further illustrate these results (Figure 4). During June 9 to 13, the A-waves arrived at
284 about the same time each day while from June 14-18, they arrived about an hour later
285 each day. This result, that the A-wave arrival times were constant early in the fortnightly
286 tidal cycle but delayed an hour per day as the waves increased in amplitude later in the
287 cycle was consistent with the model results of [Chen et al., 2013]. Wave A7 on June 15
288 was anomalously late by about 2 hours relative to waves A6 and A8.   This is attributed
289 to the passing of tropical storm Hagabus on June 14-15 with accompanying strong wind-
290 forced currents and upper ocean mixing. The B-wave arrivals began at about 20:00 on
291 June 13, and were subsequently delayed about an hour per day, similar to the
292 corresponding A-waves (Figure 4). The difference in the arrival times between the B-
293 waves and the A-waves was 6:30, 8:25, 6:15, and 5:50 on June 14-17 respectively. Wave
294 B7 was not delayed by the storm, which provides further evidence for different
295 propagation paths for the B-waves vs. the A-waves. On June 16-18 two A-waves of near
296 equal amplitude arrived about 2 hours apart. These "double A-waves" appeared over the
297 slope only near spring tide in the Luzon Straits, and the second one has been designated
298 by a prime. The origin of these waves is unclear. We speculate that the new A' waves
299 originated from a different (third) source in the Luzon Straits that is only active under
300 maximum barotropic forcing. More observations in the source region are needed to
301 understand the wave generation issues, including this double a-wave phenomenon.
302
303
304 *3.3 Wave Transformation Over the Slope*
305
306 Many significant wave transformations were observed between the 386 m (YPO2)
307 and the 266 m (RPO) isobaths over the upper continental slope. Three sections of
308 the record are shown to illustrate different phenomena. The first sequence from
309 June 2 to 6 (Figure 5) evolved out of moderate and decreasing forcing in the Luzon
310 Strait (Figure 3). The observations captured the local steepening and breaking of
311 the tidal front to form b-waves as it shoaled. The internal tides at YPO2 were
312 diurnal and nearly sinusoidal with an amplitude of about 4°C (blue line). The a-

313 waves were already evident at YPO2, but not the b-waves. Then, beginning at YPO1
314 and continuing to CPO, the leading edge of the tidal front became very steep with a
315 temperature change of 1°C / min for 5 minutes at CPO (black ellipses in Figure 5).
316 This front subsequently broke and formed b-wave packets b2 and b3 observed at
317 mooring RPO. This example thus demonstrates a local b-wave formation process
318 via steepening of the leading edge of the tidal front. This steepening temperature
319 front was due to velocity convergence at the head of the westward-propagating
320 internal tide. The formation of a similar bore-like feature at shallower depths (200
321 m – 120 m) was noted in the ASIAEX data [Duda et al., 2004] but they did not make
322 the connection to b-wave formation. Waves a1 and a2 lost amplitude and formed
323 packets as they shoaled between YPO2 and RPO. This process will be compared
324 with some recent theoretical ideas in the discussion section. Wave a3 was small at
325 YPO2 but gained amplitude as the tide progressed up the slope. This is because the
326 barotropic forcing in the Luzon Strait was weaker on June 5 than on June 2-4 (Figure
327 3). All the waves subsequently disappeared on June 7-8 during neap tide in the
328 Luzon Strait.
329
330 The second sequence during June 10-14 shows well developed A-wave packets
331 which originated from moderate but increasing remote forcing (Figure 6). Only A-
332 waves were observed until June 13 when the B-waves started to arrive. Wave B6
333 was weakly perceptible at YPO2 and increased in amplitude across the slope. The
334 temperature fluctuations induced by the A-waves increased across the slope and
335 reached a maximum of 7°C on June 11 at A3. The temperature gradients in the wave
336 fronts were again very steep, 1°C / min. The number of waves per packet increased
337 towards shallower water, most clearly in waves A2, A3, and A4. Two extraneous
338 solitary waves appeared trailing wave A5 on June 13 at CPO and RPO but were not
339 part of the A5 packet structure. Two similar waves appeared the next day trailing
340 wave A6 (Figure 7) and their origin is unclear.
341
342 The final sequence from June 14 to 18 was obtained during a period of maximal
343 forcing near spring tide at the source, and a very complicated field of NLIW emerged
344 (Figure 7). The B-waves were large and were evident at all the moorings. Wave B8
345 and B9 were solitary at YPO2 but had many waves per packet by the time they
346 reached RPO. The arrival timing was the same as the locally formed b-waves
347 (Figure 5) suggesting similar dynamics but faster/shorter development
348 time/distance when the forcing at the source was stronger. The A-waves continued
349 to grow at YPO2 during June 14-18. Interestingly, the temperature fluctuations due
350 to the largest waves did not increase monotonically as they traveled up the slope
351 from YPO2 to RPO. This is more clearly seen in a bar graph showing the maximum
352 amplitude of the isotherm of maximum displacement (Figure 8). Smaller waves
353 (June 9-12) gained amplitude as they shoaled. All waves larger than about 50 m
354
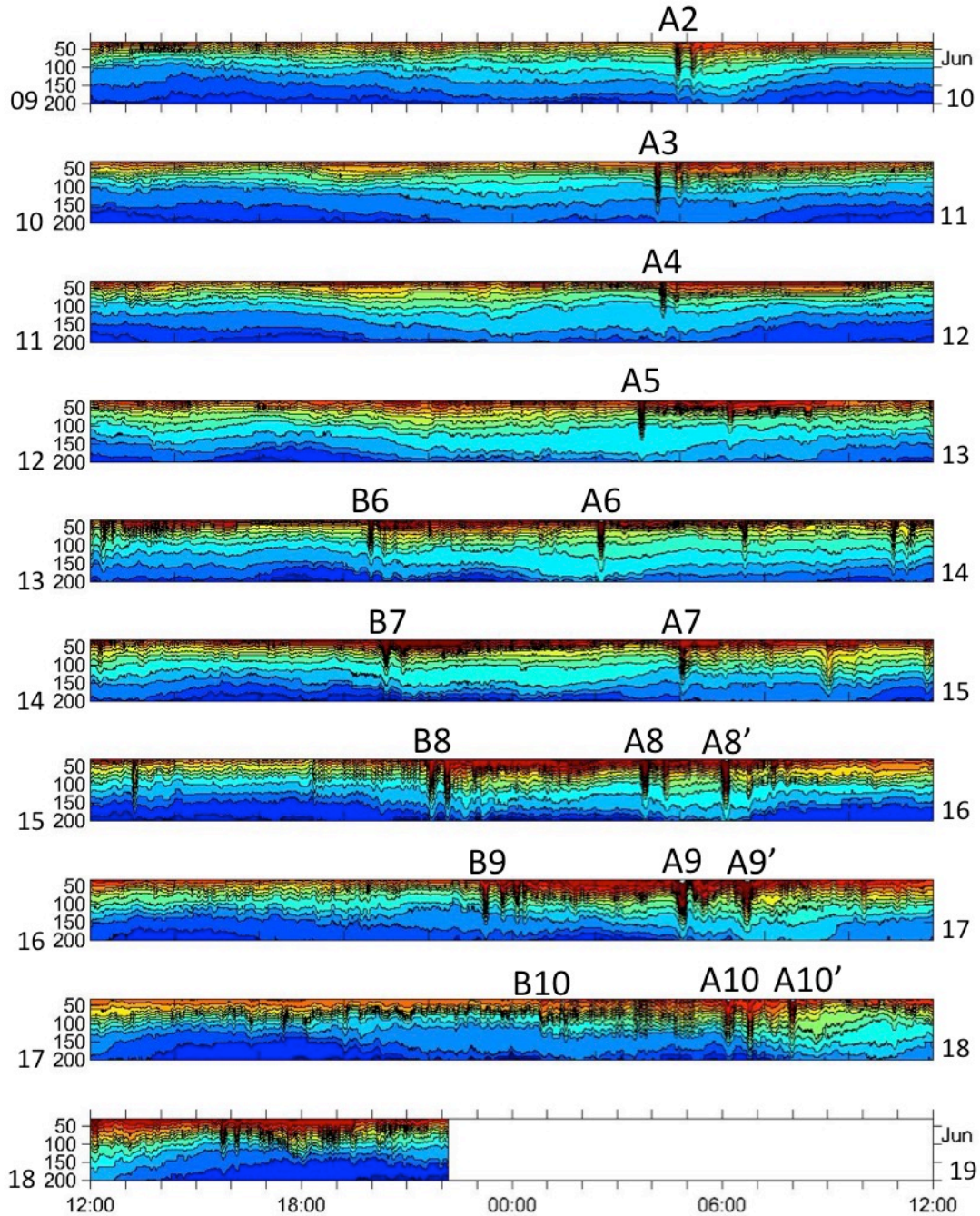
355
356
357 *Figure 4. Temperature contour plots for mooring RPO from June 9 to 19, 2014. Each*
358 *panel from top to bottom is one day centered on midnight, to capture both the A- and*
359 *B-wave arrivals. The A-waves were prominent throughout this fortnightly cycle. The*
360 *B-wave arrivals began on June 13, five days after the A-waves. The double A-waves*
361 *(A8'-A10') arrived only during June 16-18. This and similar plots were used to label*
362 *the waves in Figure 3.*
363
364
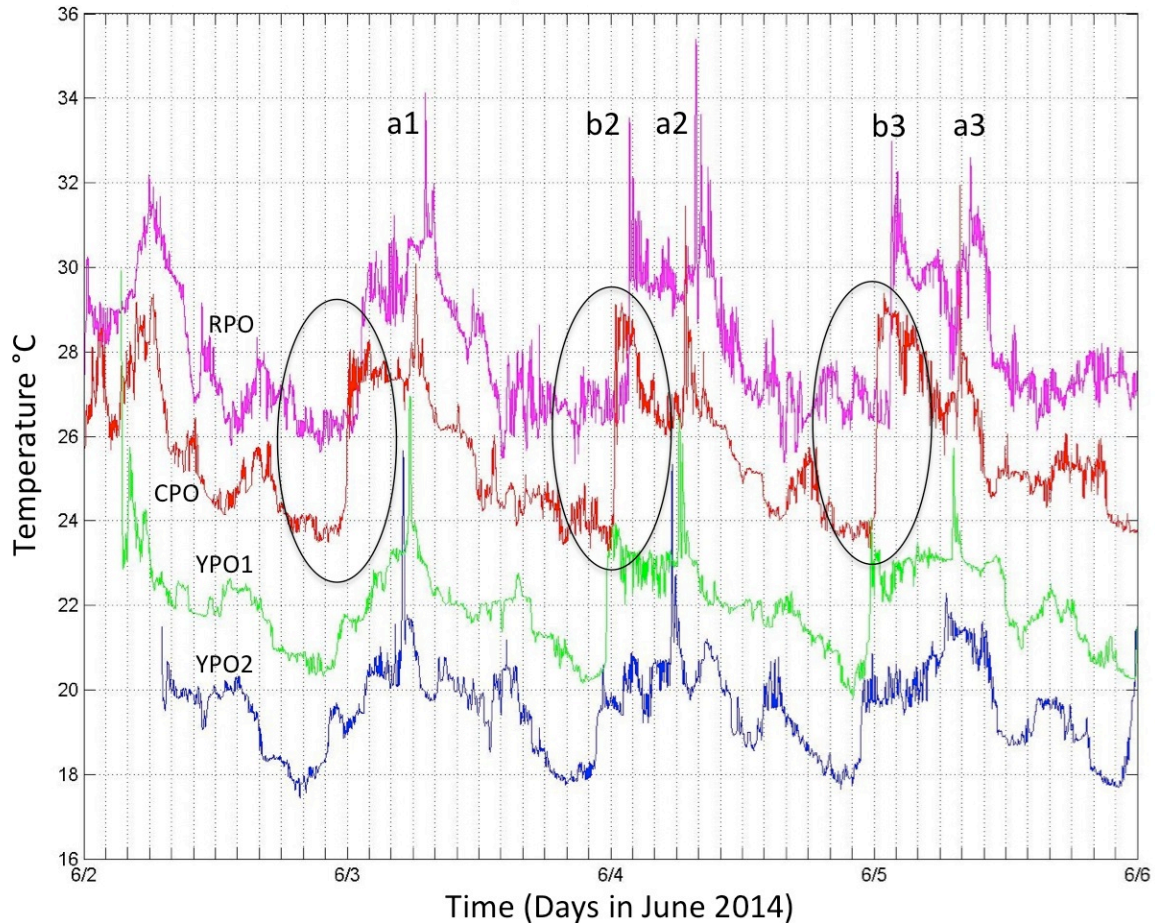
365
366
367
368 *Figure 5. Temperature vs. time during June 2-6 at all four moorings across the*
369 *continental slope. The observations are from 75m, 79m, 97m, and 99m from moorings*
370 *RPO, CPO, YPO1, and YPO2 respectively. Each time series has been offset vertically by*
371 *2 ℃ for clarity. The black ellipses highlight the region of strong temperature fronts at*
372 *CPO that subsequently broke and formed b-waves at RPO.*
373
374 offshore (June 13-18) lost amplitude as they shoaled, most clearly between CPO and
375 RPO, where the biggest change in bottom depth and slope occurred. This result is
376 consistent with the numerical results of [Lamb and Warn-Varnas, 2015] who also
377 found that smaller amplitude waves continued to gain amplitude into shallower
378 water but the larger waves did not. This fundamental result, that NLIW first gain
379 amplitude and then lose it as they shoal, is consistent with EKdV theory [Small,
380 2001; Vlasenko et al., 2005]. Note that all the wave amplitudes (Figure 8) were
381 smaller than those observed previously over the continental slope 44, 87, and 145
382 km to the southwest [Ramp et al., 2004; Lien et al., 2014; Chang et al., 2021a; Ramp
383 et al., 2022]. This is because, as seen in hundreds of satellite images (typified by
384 Figure 9), the NLIWs have maximum amplitude in the region just north of the
385 Dongsha Plateau near 20°N decreasing both northward and southward from there.
386 Along-slope observations have also shown a reduction in the upslope energy flux

387
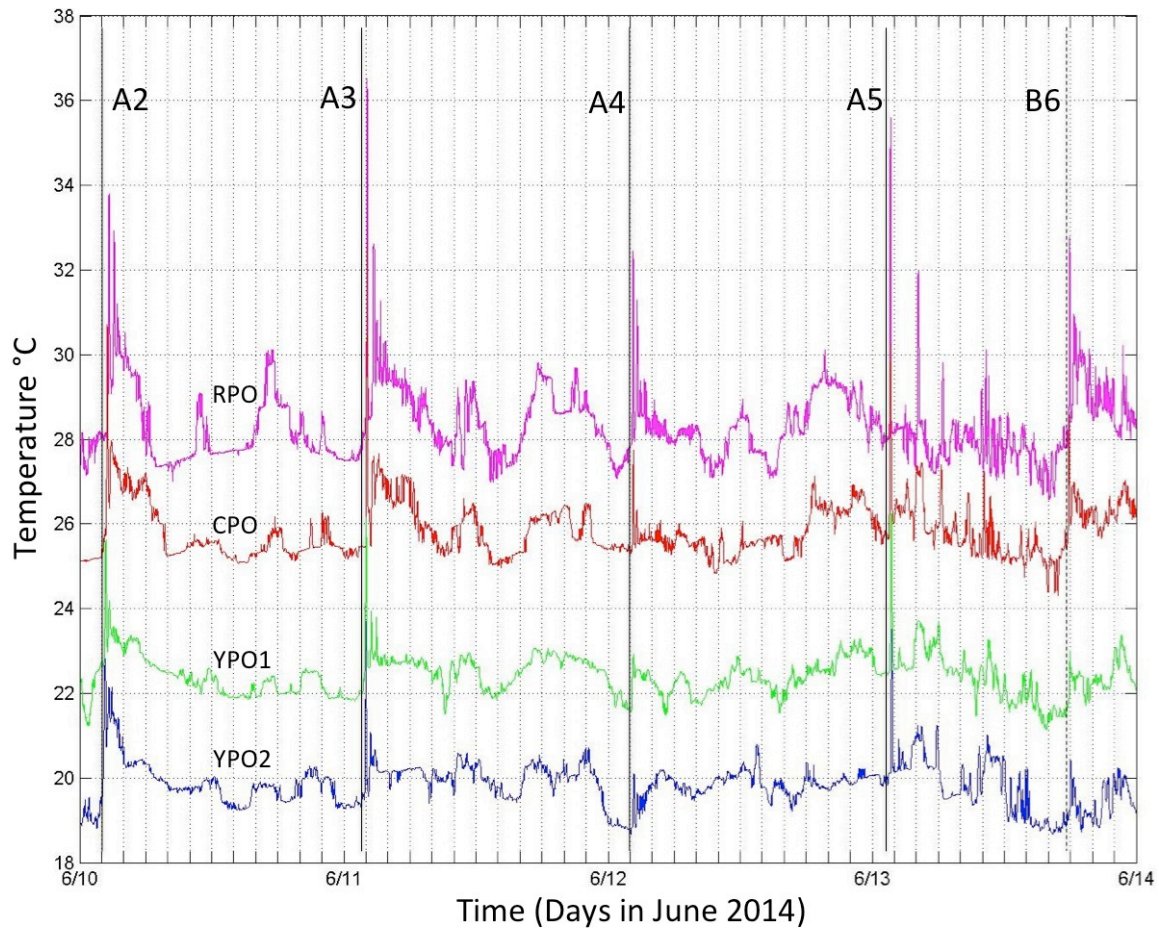
388
389
390 *Figure 6. As in Figure 5, except during June 10-14, 2014. In this plot, the time series*
391 *have additionally been shifted relative to YPO2 by the propagation time between*
392 *moorings so that individual waves line up. The lag times used are 36.5 min for YPO1,*
393 *66.8 min for CPO, and 122.8 min for RPO.*
394
395 off-axis towards the northeast [Chang et al., 2006]. The Sand Dunes site is near the
396 northeastern extremity of the wave crests as viewed in the imagery: a bit farther to
397 the northeast the waves vanished. A practical ramification of this is that the
398 undersea sand dunes were located in a region where the forcing due to encroaching
399 NLIWs was not maximal. Other factors such as the bottom slope and sediment
400 supply must also play an important role in determining the dune formation location.
401
402 The double A-wave phenomenon mentioned earlier (Figure 4) was again evident in
403 Figure 7. These waves differed from the smaller waves trailing A5 and A6 in that
404 they were already well-developed by the time they arrived at YPO2. As in Figure 6,
405 many waves which were solitary at YPO2 formed packets as they crossed the array.
406 Waves B9, A9, and A9' can be clearly seen in the satellite ocean color imagery
407 (Figure 9). The timing of the imagery at 0310 was conveniently just as wave A9 was
408
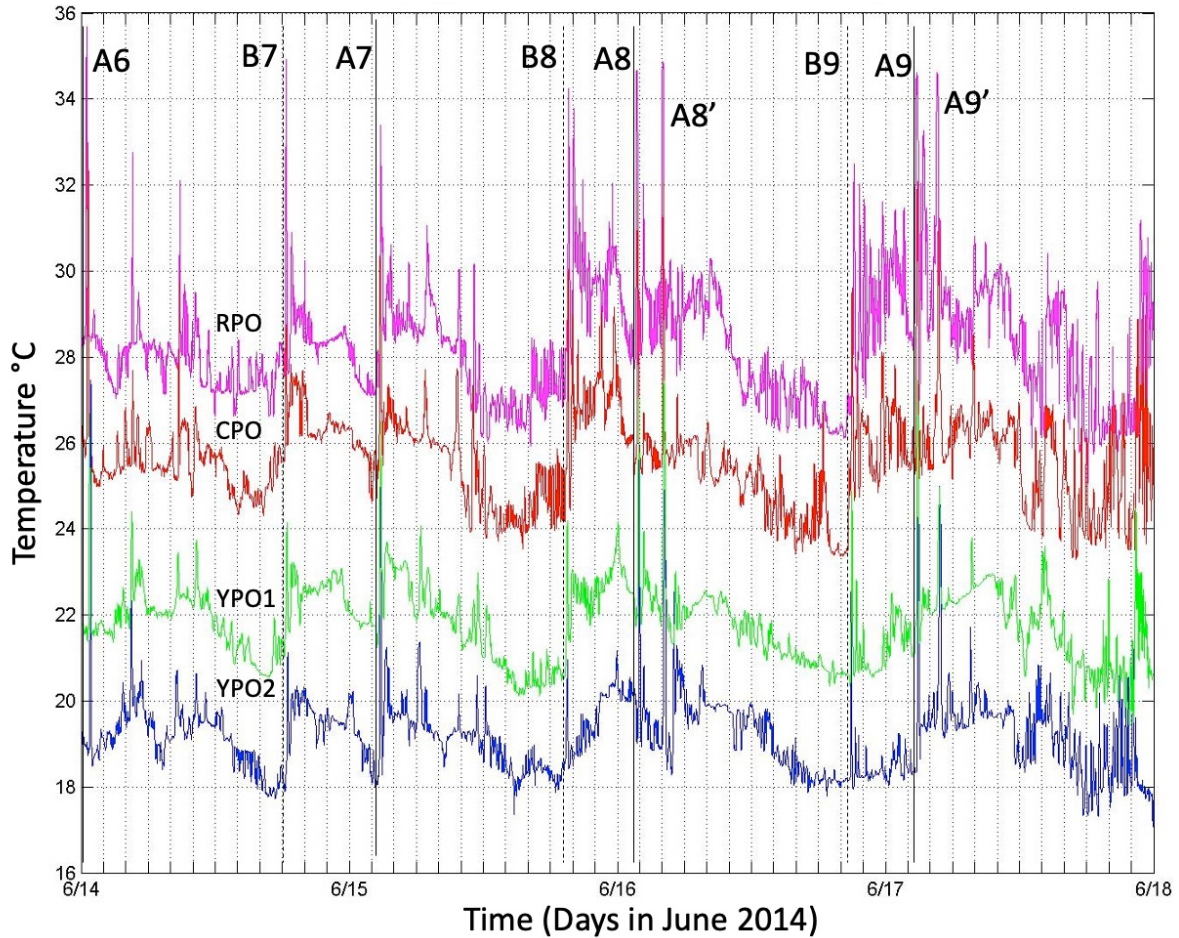
409
410
411
412 *Figure 7. As in Figure 6 except for June 14-18.*
413
414 impacting mooring YPO2. The B-wave packets and solitary nature of A9 and A9' are
415 easily seen in the image.
416
417 Two examples of velocity and temperature across the slope are shown to illustrate
418 the difference between weakly and strongly forced waves. Mooring YPO1 is not
419 shown since it was very similar to mooring YPO2 (Figure 10). The weaker case
420 begins at YPO2 on June 3-4 (Figure 10, column 1) which shows a clear a-wave near
421 0530 but no b-wave. Wave a2 was observed towards the rear of the
422 northwestward-propagating internal tide (blue near the surface). The a-wave was
423 traveling NW near the surface and in the opposite direction in the lower water
424 column, with a nodal point near 100 m. While not obvious in temperature, the
425 velocity plots show a weak second wave about 20 min behind the lead wave forming
426 a 2-wave packet. By mooring CPO (column 2), located 7.3 km away, the leading edge
427 of the internal tide had steepened to form a sharp front in both velocity and
428 temperature near midnight on June 3. There was strong convergence in the upper
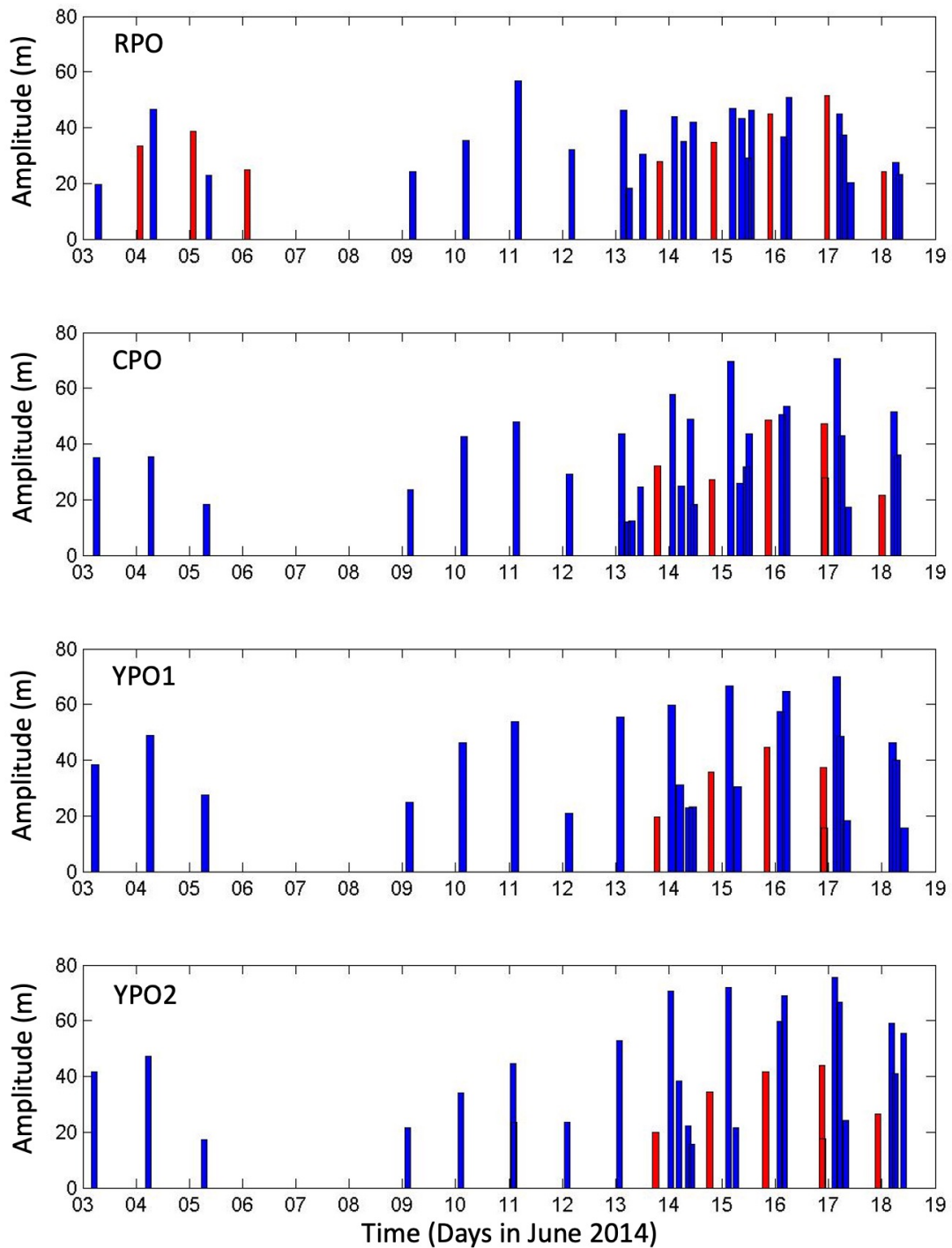
429
430
431 *Figure 8. Bar graph of wave amplitudes across the slope. The amplitudes were*
432 *calculated as deviations of the 20 °C isotherm from its mean position. The a-waves are*
433 *indicated by blue bars and the b-waves by the red.*
434
435
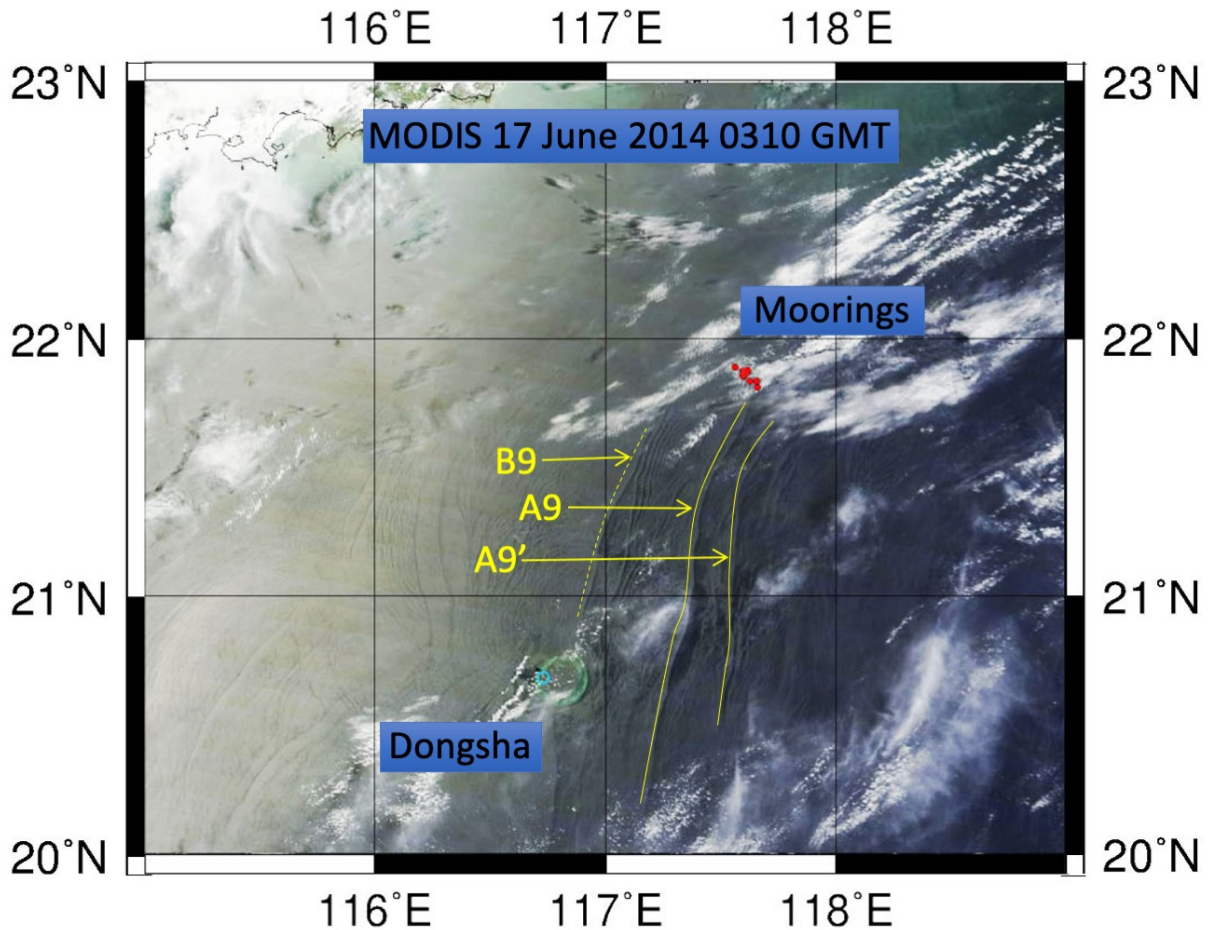
436
437
Figure 9. *A sea surface ocean color image obtained at 0310 on June 17, 2014 from the*
438 *Moderate Resolution Imaging Spectroradiometer (MODIS). The Sand Dunes moorings*
439 *are indicated by the red dots. The site of the former ASIAEX and WISE/VANS mooring*
440
441 *S7 is indicated by the yellow triangle. The surface signatures of NLIWs B9, A9, and*
442 *A9'are indicated by the yellow arrows. Wave A9 was impinging upon mooring YPO2 at*
443 *this moment, as seen in Figure 7.*

444
445 50 m with eastward flow (red shades) ahead of the front and westward flow (blue
446 shades) behind it. A solitary b-wave appeared on this convergent front which was
447 absent at YPO2. Wave a2 at CPO looked similar to YPO2, perhaps slightly stronger.
448 By mooring RPO, 5.7 km and 80 m farther up the slope (column 3), the b-wave
449 increased in amplitude and formed a 2-wave packet, and the leading a-wave
450 spawned a 4-wave packet. These waves were particularly clear in the v-component
451 since the waves refracted towards the north as they propagated up the slope (Figure
452 1). The nodal point remained near 100 m for all the leading waves. Note that the
453 background internal tide (most easily seen in the deep water) was diurnal at
454 moorings YPO2 and CPO but became more semidiurnal at RPO. This indicates the
455 presence of a locally generated tide at RPO where the bottom slope was steeper than
456 at the other moorings farther offshore. In fact, the bottom slope at YPO2-CPO
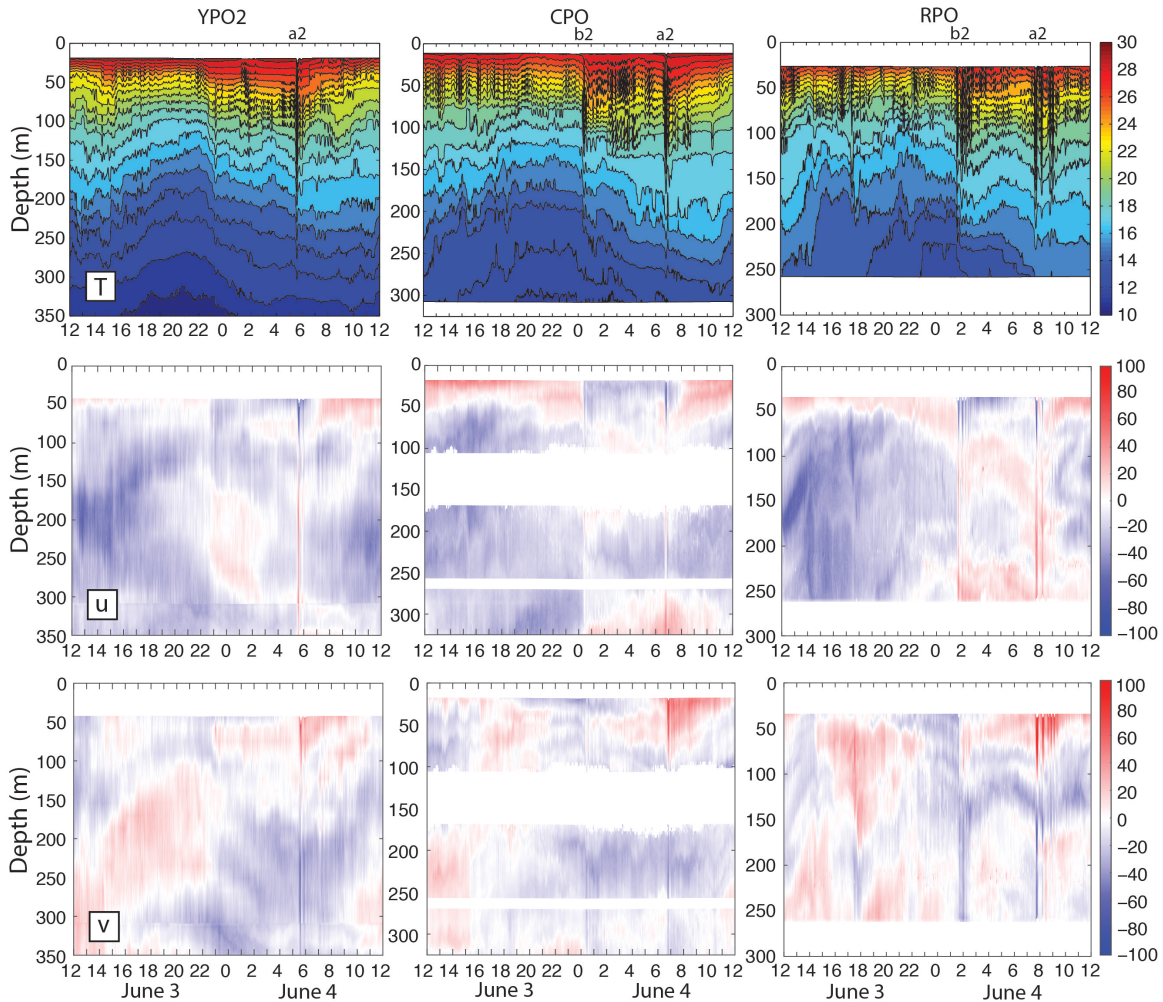
457
458
Figure 10. Temperature (top), u-component of velocity (middle) and v-component of
velocity (bottom) from 3-4 June 2014 from moorings YPO2 (left), CPO (center), and
RPO (right). The wave propagation time between moorings was 67 min from YPO2 to
CPO, and 56 min from CPO to RPO. Positive (u, v) represents (east, north) respectively.
White space at mooring CPO indicates regions not sampled by the three ADCPs. These
data were obtained during a period of moderate and declining tidal forcing, see
Figures 3 and 5 for context.

(Figures 1, 2 right of the dotted white line) was critical to the diurnal tide while the
slope at RPO (left of the dotted white line) was critical to the semidiurnal tide. The
interaction of the tidal currents with the bottom is maximal where the slope of the
tidal beams parallels the bottom and this likely contributes to the different nature of
the sand dunes offshore vs. onshore of the dotted white line (Figure 2).   At all
moorings, there was only one westward surface internal tide per day. The b-waves
all emerged at the leading edge of this westward tide, while the a-waves emerged
towards the rear, and this clear velocity signature represents another way to
distinguish the two types of waves. The two wave arrivals were separated by 6:20

476 on this day. The strongest bottom velocities were down-slope (southeast) and were
477 greater in the NLIW than in the internal tide.
478
479 The strong example (Figure 11) shows that unlike the previous example, both the B-
480 wave packet and the A-wave packet had already formed by mooring YPO2 on June
481 16-17. (Remember there is no dynamical significance to upper vs. lower case a, b:
482 the lettering is chosen to remain consistent with the nomenclature established in
483 the earlier figures and refers to the first and second cluster.) The waves were
484 traveling in the same direction as the June 3-4 waves, but had a deeper nodal point
485 located near 120-130 m. The A-wave in this case was a double A-wave mentioned
486 earlier. These resembled individual waves rather than a packet in the usual sense.
487 The two waves A9 and A9' were about the same amplitude: on this day the first
488 wave (A9) was slightly larger, but the opposite was true the day before (not shown).
489 The A9' wave was slightly wider than the A9 wave. This may be due to constructive
490
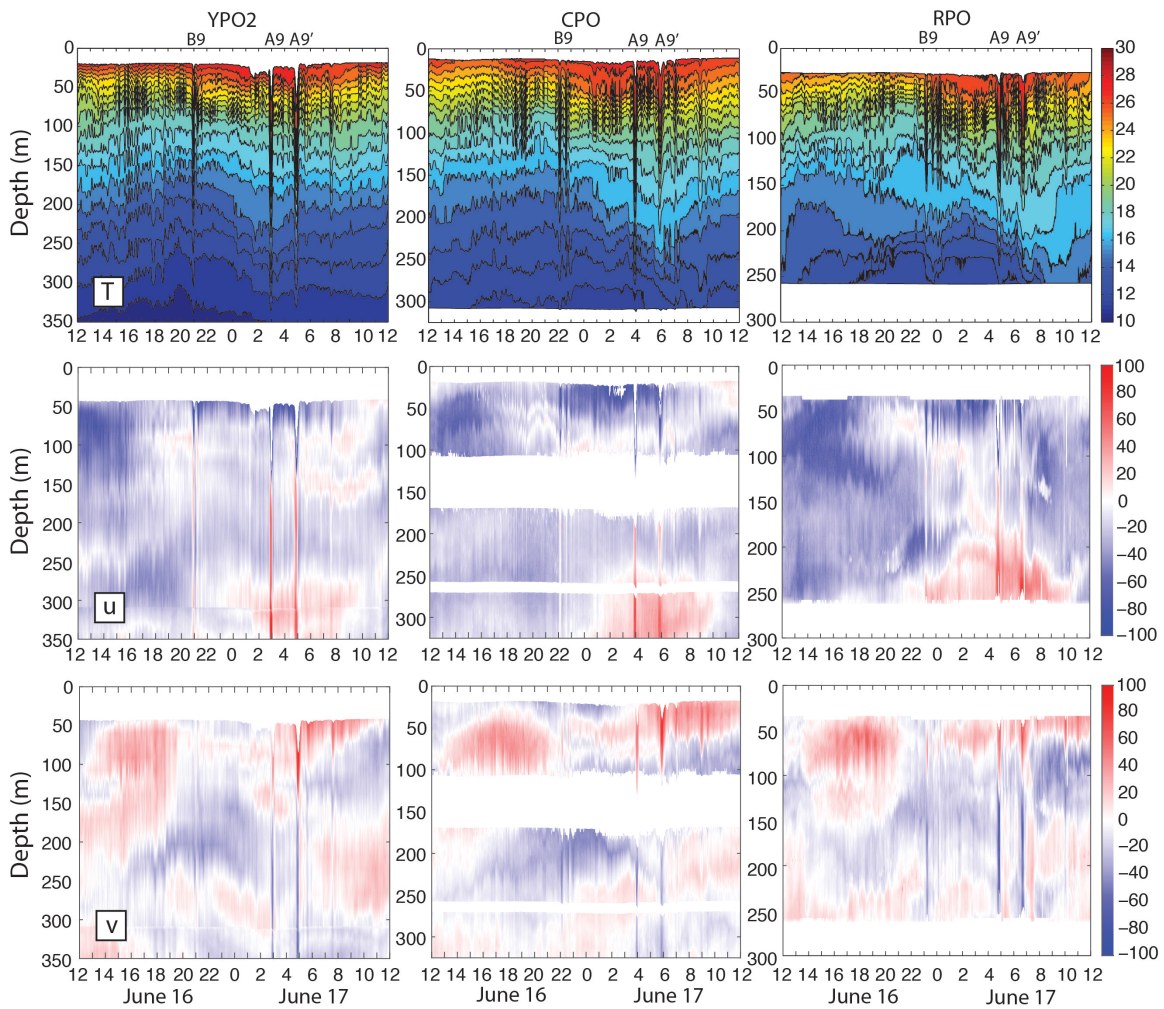
491
492
493 *Figure 11. As in Figure 10, except for June 16-17, 2014. These data were obtained*
494 *during a period of strong tidal forcing, see Figures 3 and 7 for context.*
495

496   interference with the tail of wave A9 which was just two hours ahead of it. Wave B9
497   formed a 2-wave packet at CPO (column 2) and a 3-wave packet at RPO (column 3).
498   Wave A9 formed a 2-wave packet between moorings CPO and RPO. As before, the u-
499   component shows the B-wave was coming off the leading edge of the westward
500   surface tide (eastward bottom tide). The A9 wave grew out of the middle of the tide
501   and the A9' wave emerged from the trailing edge of the same westward internal
502   tide. The surface westward velocities exceeded 97 cm s^{-1}, 162 cm s^{-1}, and 153 cm s^{-1}
503   at YPO2, CPO, and RPO respectively. The eastward bottom velocities exceeded 20
504   cm s^{-1}, 85 cm s^{-1}, and 80 cm s^{-1} respectively. The smaller lower layer velocities
505   below the nodal point were consistent with a thicker lower layer and with theory
506   [Lamb and Warn-Varnas, 2015]. The strongest bottom velocities outside the waves
507   were about half the wave velocities. Clearly the strongest bottom velocities
508   observed over the upper continental slope were generated by the passing NLIWs,
509   although these high velocities were very brief compared to the internal tide.
510   Referring once again to Figure 8, the B-wave (just before midnight on June 16)
511   started at YPO2 with just over 40 m amplitude and grew shoreward across the shelf.
512   In contrast, the much larger A-waves just after midnight on the 17th started out
513   with 70 – 75 m amplitude at YPO2 and lost amplitude across the shelf. This is
514   consistent with the earlier discussion surrounding Figure 10.
515
516   Many ordinary internal waves can be seen in Figure 11 in between the nonlinear
517   waves. These waves were likely generated by tropical cyclone Hagabus which
518   passed over the array on June 14-15 with winds exceeding 25 m s^{-1}.
519
520   On June 16 a packet of convex mode-2 waves appeared from 1500-2100 centered
521   near 60 m and extending from 50 to 100 m depth (Figure 11, bottom row). These
522   waves strengthened upslope from YPO2 to RPO and trailed the double-A waves
523   from the day before (not shown). There looked to be about 6 waves in the mode-2
524   packet at mooring RPO. All three of the double-A waves on 16, 17, and 18 June had
525   this feature associated with them. The observation is consistent with [Yang et al.,
526   2009, 2010] who observed mode-2 waves trailing mode-1 waves in the ASIAEX
527   region nearby and attributed this to the adjustment of shoaling mode-1 waves.
528   These observed wave transformations are now discussed further below in light of
529   the theory for shoaling solitary waves.
530
531   **4 Discussion**
532
533   *4.1 Theoretical Framework*
534   In this section, the observed NLIW characteristics are compared with laboratory and
535   numerical studies to determine what kind of changes might be expected as the waves
536   shoal over the sand dunes region. The possibilities include adiabatic shoaling, dispersion,
537   breaking, and conversion to waves of elevation. The latter may be easily ruled out for
538   this study since this only happens when the nonlinear coefficient α from the KdV
539   equation changes sign, which typically takes place between $100 - 120$ m depth over the
540   Chinese continental shelf [Hsu and Liu, 2000; Orr and Mignerey, 2003; Liu et al., 2004].

541   Even accounting for some temporal variability due to the local internal tides, this "critical
542   point" where the upper- and lower-layer depths were equal was always well inshore of
543   the sand dunes region.

544   The wave progression WNW from deeper to shallower water may be conveniently
545   framed in terms of the two regions demarcated by the dotted white line in Figure 2.
546   Moorings YPO1, YPO2, CPO were all located in the region where the mean bottom slope
547   was .006 = 0.6% = 0.3. Mooring RPO was in the region where the bottom slope was 0.03
548   = 3% = 1.7 degrees. The bottom slope is considered gentle when it is less than 0.03 =
549   1.7° [Grimshaw et al., 2004; Vlasenko et al., 2005; Lamb and Warn-Varnas, 2015;
550   Rivera-Rosario et al., 2020]. Dynamically speaking then the mean bottom slopes in the
551   sand dunes region ranged from weak to practically flat. Under these conditions, the
552   response of shoaling NLIWs depends primarily on three factors: the bottom depth, wave
553   amplitude, and thermocline depth [Small, 2001; Vlasenko and Hutter, 2002; Lamb, 2002;
554   Vlasenko and Stashchuk, 2007; Grimshaw et al., 2014; Lamb and Warn-Varnas, 2015;
555   Rivera-Rosario et al., 2020]. Waves break when wave orbital velocity u_{max} > the
556   propagation speed c [Lien et al., 2014; Rivera-Rosario et al., 2020; Chang et al., 2021b]
557   and

558                                $$a_m > (H_b - H_m)0.4 \qquad\qquad\qquad (1)$$

559
560   where a_m is the maximum possible wave amplitude, H_b is the bottom depth, and H_m is the
561   upper layer thickness, here approximated by the thermocline depth [Helfrich and
562   Melville, 1986; Helfrich, 1992; Vlasenko and Hutter, 2002]. This expression can be used
563   to evaluate the isobath where a wave of given amplitude will break, or alternatively, to
564   determine the wave amplitude necessary for wave breaking at a given isobath. For the
565   Sand Dunes data set, these criteria were examined for moorings CPO in region 1 and
566   RPO in region 2. The depth of the 23°C isotherm was used to estimate the thermocline
567   depth at both moorings. The undisturbed isotherm depth, determined by time-averaging
568   the low-pass filtered data, was similar at both moorings, 60 m at CPO and 57 m at RPO.
569   Substituting these values in (1) shows that a wave amplitude of 112 m would be required
570   at CPO for wave breaking to occur. Moving on to RPO, the required amplitude for wave
571   breaking there would be about 84 m. Comparing with the observed wave amplitudes at
572   CPO and RPO (Figure 8), all the observed wave amplitudes were less than the above
573   criteria, and no wave breaking events are expected in this array. Some combination of
574   adiabatic shoaling and packet formation via wave dispersion is more likely instead.
575
576   Using this guidance, the temperature and velocity structure at site RPO is studied in
577   greater detail for three examples: a statistically common a-wave (Figure 12), a very
578   large a-wave (Figure 13) and a b-wave (Figure 14). For wave A3 on June 11 (Figure
579   12), which typifies A-waves between June 3-13, the wave was symmetric in both
580   velocity and temperature with no sign of back-side steepening. The wave amplitude
581   was 57 m, and the maximum orbital velocity was 1.04 m s^{-1} and was located near
582   the surface. This was much less than the local propagation speed of 1.60 m s^{-1}. The
583   opposing lower layer velocity was order 0.75 m s^{-1} commensurate with the thicker
584   lower layer. Such bottom velocities were commonly observed and are easily enough

585 to produce both bedload and suspended sediment transport among the dunes
586 [Reeder et al., 2011]. The w-profile was nearly symmetric at ± 0.25 m s^{-1}, downward
587 ahead of the wave and upward behind it, with the maxima located near mid-depth.
588 One or possibly two trailing waves were observed: the first was centered near 4:48
589 and had vertical velocities of ± 0.8 m s^{-1} while the second was near 5:00 with
590 vertical velocities of just a few cm s^{-1}. A fourth wave-like feature was observed in
591 the temperature plot near 5:20 but it cannot be discerned in the velocity structure.
592 To summarize, wave A3 consisted of a primary wave and 2-3 trailing waves about
593 30 min behind. The wave was symmetric in velocity and temperature with no sign
594 of breaking or trapped core formation.
595
596 The largest wave observed was wave A9 on June 17. This wave showed several
597 characteristics of breaking or near-breaking waves (Figure 13). The back side of the
598 wave was steeper than the leading side, and the jagged temperature contours in the
599 wave core were indicative of breaking and/or mixing. A "pedestal" was starting to
600 form behind the wave as described by [Lamb and Warn-Varnas, 2015]. Several
601 more smaller depression waves were emerging from the "pedestal." The velocity
602 contours were likewise asymmetric and showed a subsurface maximum near 60-70
603 m which was about 0.20 m s^{-1} greater than the surface. This is typical of waves with
604 trapped cores [Lien et al, 2012, 2014; Lamb and Warn-Varnas, 2015]. The
605 maximum near-surface velocity was 1.55 m s^{-1}, which was close to the local
606 propagation speed (1.60 m s^{-1}). It is possible that the surface velocities above 20 m
607 depth were slightly larger but were not observed. At site CPO, this same wave had a
608 maximum velocity of 1.80 m s^{-1}, also very close to the local propagation speed. The
609 vertical velocities were actually smaller than wave A3, at -12 and +20 cm s^{-1} with at
610 least two and possibly more of the trailing depression waves visible as down/up
611 pairs. To summarize, this wave appears to be about to break or just starting to
612 break, however, this wave was the exception rather than the rule: only one such
613 wave was observed. It is possible that the trailing double-A waves A8' and A9'
614 might also meet these criteria, however their form was distorted by interference
615 from the trailing packet of the leading A8 and A9 waves two hours earlier, making
616 their characteristics difficult to discern. The South China Sea NLIW amplitudes in
617 June are near their maximum values observed in July and August [Chang et al.,
618 2021a]. It is thus unlikely that breaking waves are ever prevalent in the sand dunes
619 region. This situation contrasts with a similar depth range farther southwest, where
620 larger waves were already actively breaking at the 300 m isobath [Chang et al.,
621 2021b].
622
623 It is worth noting that subsurface velocity maximum in the wave may be caused by
624 phenomena other than wave breaking. Tropical cyclone Hagabus passed over the
625 array on June 14-15 and forced strong near-surface currents which opposed the
626 wave velocities. This was especially obvious on June 15 (not shown) when
627 westward currents at 80 m depth in wave A7 exceeded the surface currents by over
628 0.80 m s^{-1} at RPO and by over 1.00 m s^{-1} at CPO. This likely explains why wave A7
629 arrived 2 hours late with respect to waves A6 and A8 (Figure 4). The storm also left
630 behind a surface mixed layer 40 m deep which lingered to the end of the record.
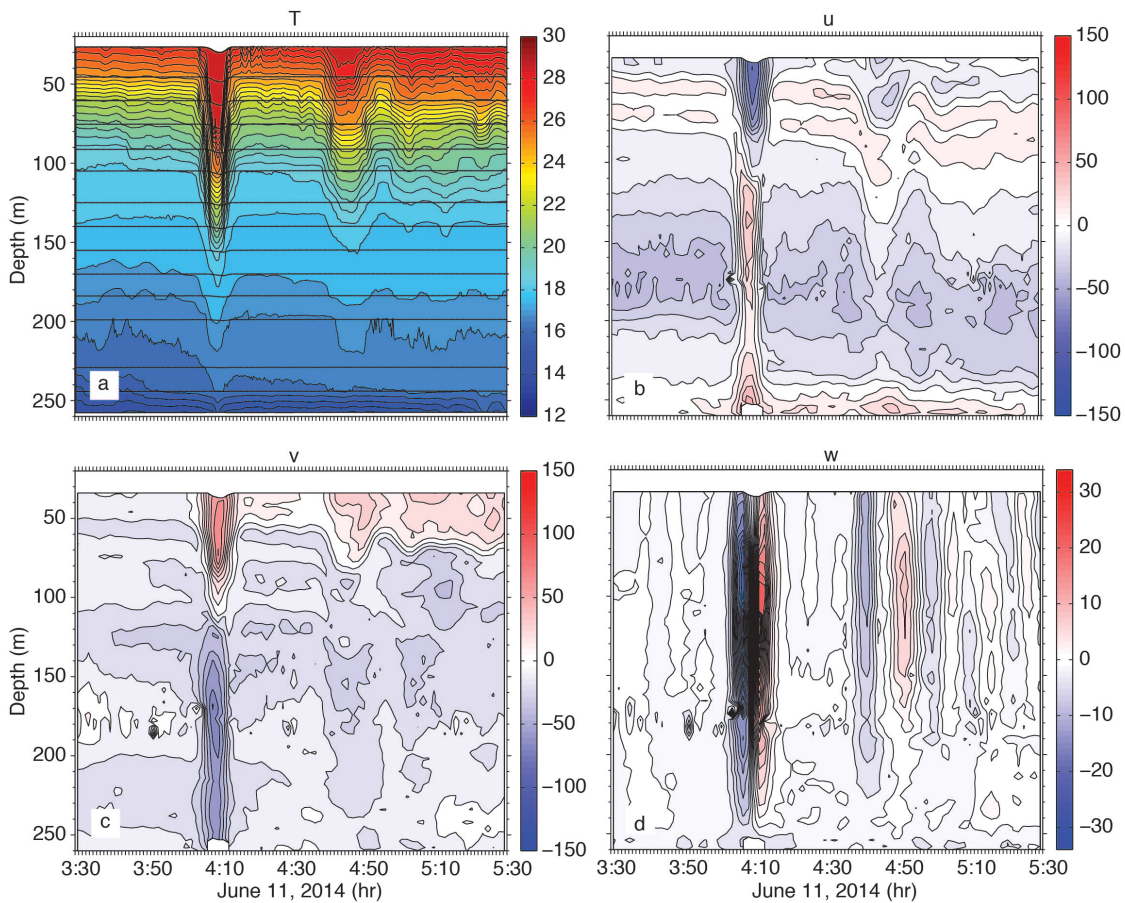
Figure 12. a) temperature, b) u-component of velocity (positive east), c) v-component of velocity (positive north), and vertical velocity (positive up) for wave A3 on June 11, 2014. This rank-ordered packed with a symmetrical leading wave typifies most of the type-a waves observed during the experiment.

This means all the largest waves forced near spring tide propagated into a region with an unusually deep surface mixed layer. The effect of this is to severely limit wave breaking [Lamb, 2002]. In fact, the scenario described above in the results section rather closely resembles the model results of [Lamb, 2002] when a surface mixed layer was added (their Figure 10). The shoaling solitary wave in the model produced a second trailing solitary wave, followed by the dispersive tail of mode-1 depression waves, followed by a packet of mode-2 waves. The observations reported here closely resembled this pattern not only on June 16-18, but also on June 3-5 trailing waves a1 and a2.

We conclude that most of the packets that formed as the waves traveled up the slope from YPO2 to RPO were formed by dispersion rather than wave breaking. Rotational effects seem locally unimportant, given that the packets formed in just two hours while the local inertial period was 32 hours. Rotation may have played a

654
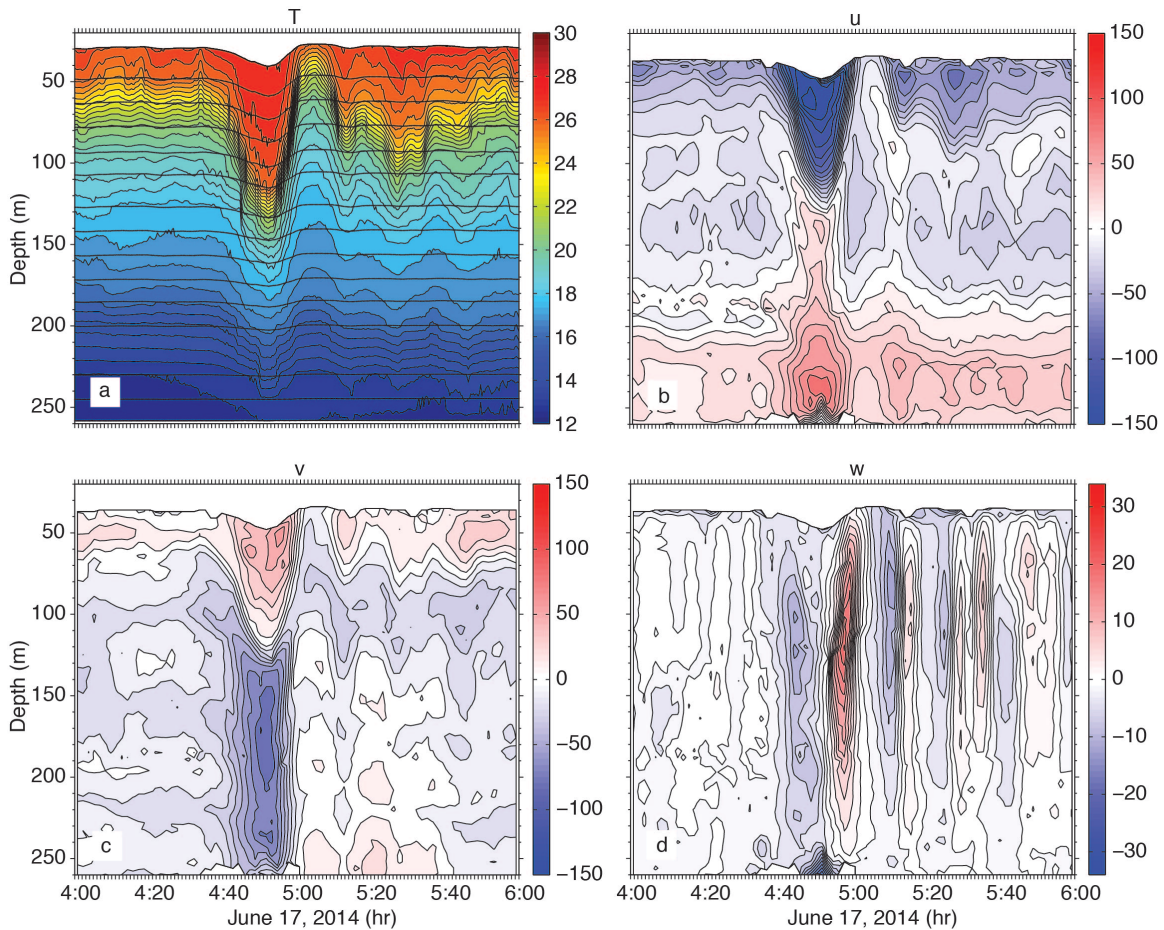
655
656
657
658 *Figure 13. As in Figure 12, but for wave A9 on June 17, 2014. The steepening back side*
659 *and subsurface velocity maximum suggest breaking or imminent breaking.*
660
661 role farther offshore, establishing the initial perturbations (inertial gravity waves)
662 that then grow and become a trailing packet as the waves shoal [Grimshaw et al.,
663 2014]. This effect could not be investigated without observations in deep water.
664 Trailing undular bores of the sort modeled by [Grimshaw et al., 2014] by including
665 rotation were not observed, but are likely not observable since in the real ocean, the
666 waves arrive periodically and the trailing undular bores would be destroyed by each
667 subsequent arriving NLIW before they have a chance to develop. It is most likely
668 then an imbalance between nonlinearity and dispersion that causes the new trailing
669 waves to form [Vlasenko and Hutter, 2002; Lamb and Warn-Varnas, 2015]. The
670 large lead ISW in the Sand Dunes array never split in two, but rather slowly
671 decreased in amplitude as energy was transferred to the dispersive tail. Phenomena
672 such as wave splitting and breaking likely took place inshore of the sand dunes
673 array in the vicinity of the 150 m isobath, as was observed previously at the ASIAEX
674 site nearby.
675
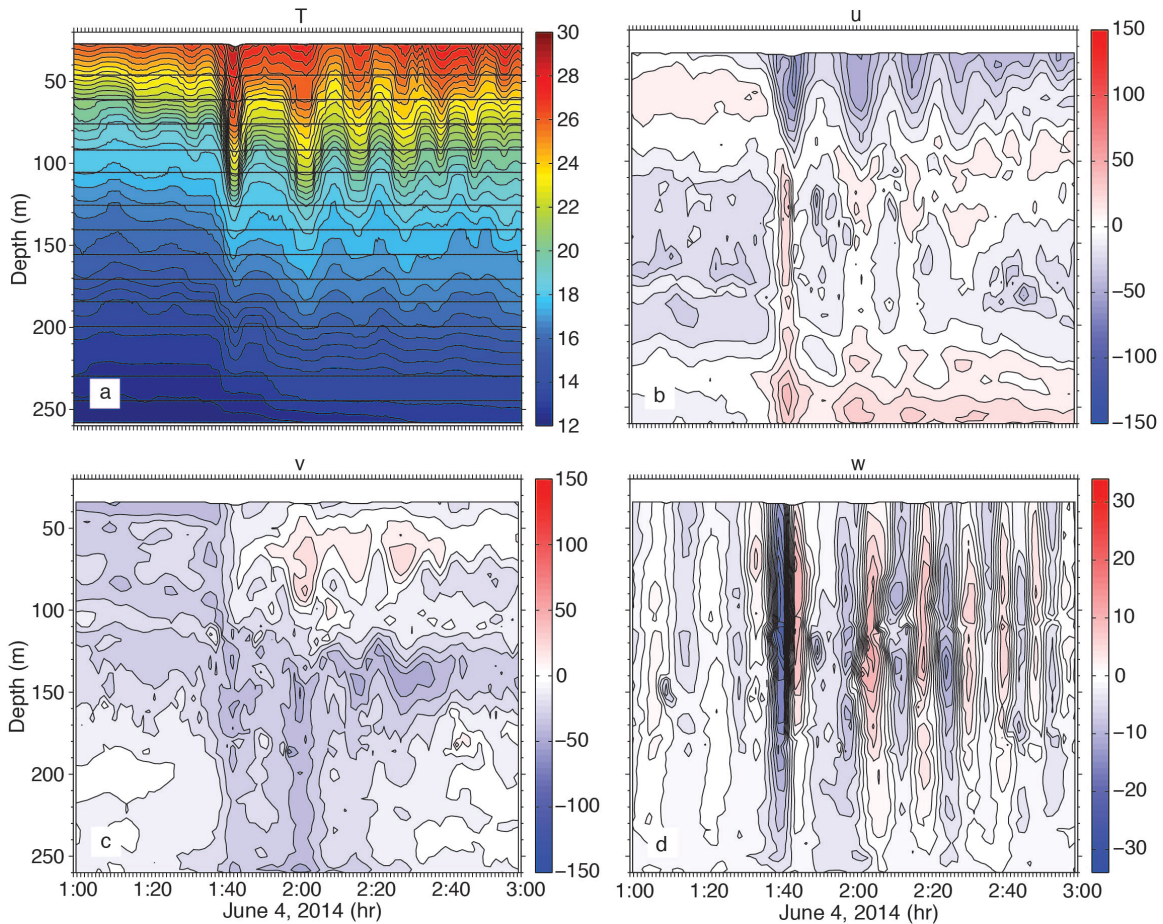
Figure 14. As in Figure 12, except for wave b2 on June 4, 2014. This example typifies waves formed locally by breaking of the tidal front between moorings YPO and RPO.

The situation for the locally formed b-waves (b2-b4) was completely different. These waves were non-existent at YPO2 but formed well-defined, evenly spaced packets by the time they reached RPO (Figure 14). For wave b2 on June 4, six waves can be clearly seen in T and w, with most all the horizontal velocity in u, that is these waves were traveling westward. The amplitude of the lead wave was about 40 m, the near surface velocity 60 cm s^{-1} westward, and near-bottom velocity 40 cm s^{-1} eastward. The waves were formed all at once by the collision and breaking of the westward internal tide with the off slope propagating eastward tide. This is a different mechanism than that described for shoaling ISWs in the literature.

4.2 Energy and energy flux

The data set provides an opportunity to observe how the horizontal kinetic (HKE) and available potential (APE) energy in the high-frequency nonlinear internal waves changes as the waves propagate up a gentle slope. In turn, the energy pathways provide some insight to the dynamics underlying the wave transformation process.

696 The theoretical expectation for linear and small-amplitude nonlinear internal waves
697 is that the energy will be equipartitioned for freely propagating long waves away
698 from boundaries. This is not the case however for finite amplitude nonlinear,
699 nonhydrostatic internal solitary waves whose KE typically exceeds the PE by a
700 factor of 1.3. This result was found theoretically via exact solutions to the fully
701 nonlinear equations of motion [Turkington et al., 1991] and has also been noted
702 observationally [Klymak et al., 2006; Moum et al., 2007]. Thus, the KE is expected to
703 slightly exceed the PE for the waves arriving at mooring YPO2. For shoaling NLIW
704 however, the flux of PE theoretically exceeds the flux of KE which causes the PE to
705 exceed the KE in shallower water [Lamb, 2002; Lamb and Nguyen, 2009]. This is
706 because the flux of PE remains nearly constant while the KE flux decreases as the
707 upper- and lower-layer thicknesses become more equal. Shoaling waves observed
708 in the Massachusetts Bay displayed this property [Scotti et al., 2006]. Thus, a shift
709 from greater KE to greater PE might be expected as the waves shoal from YPO2 to
710 RPO, although it depends on the details of the wave amplitude, stratification, bottom
711 slope, etc.
712
713 To compute the energies and energy fluxes from moorings, time series of density
714 and velocity which are uniform in space and time are required. Moorings RPO and
715 CPO had good coverage of temperature and salinity in the vertical (Appendix A)
716 however moorings YPO1 and YPO2 sampled temperature only. Two methods to
717 compute the density at YPO1 and YPO2 were explored. The first used a constant
718 salinity (34.42, the vertical average from a nearby CTD cast) paired with the
719 observed temperature at each sensor to compute density. This method assumes
720 that most of the density variability comes from the temperature fluctuations rather
721 than salinity. The second method used the salinity profiles from all the CTD casts
722 taken during the cruise to compute a mean T/S curve, which was then used as a
723 look-up table to determine the salinity to use with each observed temperature. The
724 CTD casts were all within 12 km of each other and were thus treated as a time
725 series. The profiles fell into two groups, namely before tropical storm Hagabus
726 passed by on June 14, with little-to-no surface mixed layer, and after the storm when
727 the mixed layer was about 40-50 m deep. Thus, two mean T/S curves were actually
728 used, one from before the storm and one after. The benchmark for these methods
729 was to compare the density calculated using the T/S curves with the actual density
730 calculated using the observed salinity on moorings RPO and CPO. The APE
731 computed using the mean T/S curve was found to agree much better with the
732 observations than the APE computed using a constant value for the salinity. Both
733 techniques were slight underestimates of the true APE, but the T/S method much
734 less so than the constant method. For this reason, the mean T/S curves were used
735 to compute the density time series, and thus APE for moorings YPO1 and YPO2.
736
737 The observed time series also had velocity gaps of varying severity in the water
738 column due to the range limitations of the ADCPs. Mooring CPO had a mid-depth
739 gap spanning roughly 110-170m and a second smaller gap from 255-265m (see
740 Figures 10 and 11). These gaps were filled using the least squares fit normal mode
741 techniques described in [Nash et al., 2005]. Theoretically as many as seven modes

742 (number of instruments in the vertical – 1) were possible, but the most stable
743 results were achieved with just three modes. No attempt was made to fill in the
744 upper 20 m of the water column where both velocity and temperature were
745 unsampled by the moorings.
746
747 Once clean time series were available to operate on, the energies and energy fluxes
748 were computed from the data via established techniques [*Nash et al.,* 2005, 2006;
749 *Lee et al.,* 2006]. The baroclinic velocity and pressure fluctuations induced by the
750 waves were first computed as
751

752 $$\vec{u}'(z,t) = \vec{u}(z,t) - \overline{u}(z) - \frac{1}{H}\int_{-H}^{0}\left[\vec{u}(z,t) - \overline{u}(z)\right]dz \qquad (1)$$

753
754 and
755

756 $$p'(z,t) = g\int_{z}^{0}\rho'(\xi,t)d\xi - \frac{g}{H}\int_{-H}^{0}\int_{z}^{0}\rho'(\xi,t)d\xi\,dz \qquad (2)$$

757
758 where
759
760 $$\rho'(z,t) = \rho(z,t) - \overline{\rho}(z) \qquad (3)$$

761
762 is the density anomaly with respect to the time-mean density profile. In equations
763 (1) and (2), the last term satisfies the baroclinicity requirement that the primed
764 quantities integrate to zero over the entire water column [*Kunze, et al.,* 2002]. Over
765 bars indicate temporal means. The HKE and APE can then be computed as
766
767 $$HKE = \rho_0\left(u'^2 + v'^2\right)/2 \qquad (4)$$

768 $$APE = \frac{1}{2}\frac{g^2\rho'^2}{\rho_0 N^2} \qquad (5)$$

769
770 where ρ_0 is the mean density, g is the acceleration of gravity and N^2 is the buoyancy
771 frequency.
772
773 The energy flux due to highly nonlinear internal waves is given by
774
775 $$\vec{F}_E = \vec{u}'\left(p' + HKE + APE\right) \qquad (6)$$

776
777 where the first term on the right is the pressure work and the second and third
778 terms represent the advection of horizontal kinetic and available potential energy
779 density [Nash et al., 2012]. For the small amplitude, linear, hydrostatic case the flux
780 equation is often approximated as the first term only

781

782    $$\vec{F}_E = \vec{u}'p'$$ (7)

783

784   but since it is not obvious that this approximation is valid for the strongly nonlinear
785   shoaling waves observed in the sand dunes region, all three terms of the flux
786   equation were computed.

787

788   The resulting changes in the wave energy distribution across the slope depended on
789   the wave amplitude (Figure 15). For waves up to and including A3 on June 11, the
790   APE exceeded HKE offshore and continued to increase up the slope. This is
791   interpreted to mean the waves were still growing and had not yet reached
792   maximum amplitude. Smaller waves can penetrate farther upslope adiabatically
793   than larger waves. Wave A4 was anomalously small for which no obvious
794   explanation has been found. Perhaps the wave was obliterated by the leading edge
795   of tropical storm Hagabus. Starting with wave A5 on June 13, as the remote
796   barotropic tidal forcing continued to increase, the HKE exceeded APE at YPO2 by a
797   factor averaging 1.7 and increased to its maximum value at mooring YPO1. This
798   ratio is even larger than the theoretical expectation of 1.3 [Turkington 1991; Lamb
799   and Nguyen, 2009] and indicates highly nonlinear waves with large amplitudes.
800   Between CPO and RPO, there was a dramatic change when the APE increased and
801   the HKE sharply decreased, resulting in greater APE than HKE at mooring RPO
802   (Figure 15a). The energy ratio at RPO (Figure 15f) was commonly three to four but
803   suddenly decreased sharply with the arrival of wave A6 on June 14 and remained
804   near one for the remainder of the time series. This is attributed to the increased
805   surface mixed layer depth as the tropical storm went by which wiped out the upper
806   ocean stratification and reduced the APE. The total energies (Figure 15e) integrated
807   both vertically and over a wavelength, followed an envelope consistent with the
808   remote tidal forcing and maxed out at around 250 MJ m^{-1}. This was less than half
809   the energy (550 MJ m^{-1}) previously reported over the Dongsha Plateau [Lien et al.,
810   2014] where the maximum observed wave amplitudes exceeded 150 m vs. 80 m
811   here. The total energy appears approximately conserved across the slope for many
812   of the waves as indicated by color bars of approximately equal length (Figure 15e).
813   The losses in HKE were compensated for by the increases in APE, in reasonable
814   agreement with theory and numerical simulations [Lamb and Nguyen, 2009; Lamb
815   and Warn-Varnas, 2015]. For the larger waves however, such as a1, A6, A8', A9, and
816   A9' the total energy decreased upslope (Figure 15e). The HKE was lost much faster
817   than the APE was gained. This is attributed to strong dissipation over the rough
818   bottom in the dune field [Helfrich et al., 2022].

819

820   In the simplest sense the energy flux is just the energy times the group velocity (or
821   phase velocity for non-dispersive waves). Since the phase velocity varied from 1.87
822   m s^{-1} between YPO2 and YPO1 to 1.69 m s^{-1} from CPO to RPO, the flux/energy ratio
823   is expected to vary little across the slope and the flux patterns should resemble that
824   of the total energies. This is indeed the case as seen by comparing the envelope of
825   the curves for the total flux (Figure 16b) and the total energy (Figure 15e). The
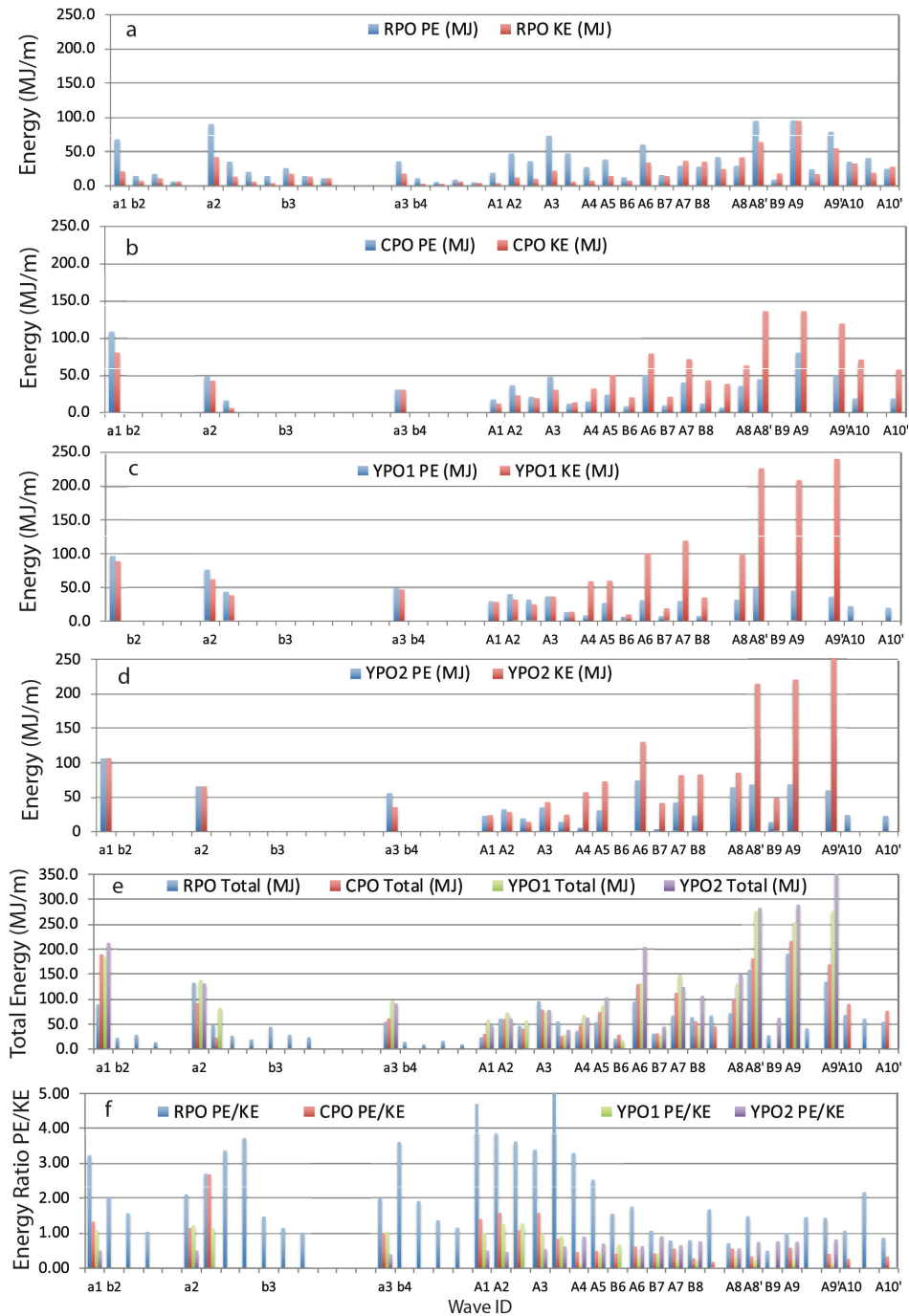
826
827
828 *Figure 15. Energy transformations across the slope. The total HKE and APE,*
829 *computed by integrating the wave energy both vertically and horizontally at moorings*
830 *RPO, CPO, YPO1, and YPO2 are shown in panels a-d respectively. The total pseudo-*
831 *energy (HKE + APE) at all four moorings is shown for each wave in panel e, and the*
832 *APE/HKE ratio in panel f.*

833 vertically integrated flux tends to decrease upslope primarily due to the decreasing
834 water depth. Of greater interest is the change in the various terms of equation (6).
835 The pressure work is indeed the largest term but not by much: The PW comprised
836 57%, 56%, 43%, and 52% of the total flux at YPO2, YPO1, CPO, and RPO
837 respectively. The large percentage still remaining was accounted for by the
838 advection of HKE and APE and shows that the waves were indeed strongly
839 nonlinear. The increase in APE with respect to HKE at mooring RPO versus CPO can
840 be accounted for by the change in the fluxes at those moorings (Figure 16a). From
841 CPO to RPO, the kinetic energy flux dropped by 50% (blue line to green line) while
842 the potential energy flux went up slightly (red line to purple line).
843
844 **5. Summary and conclusions**
845
846 An 18-day time series of high-resolution velocity and temperature data were
847 obtained at four closely spaced moorings spanning 386-266 m depth on the
848 continental slope 160 km northeast of Dongsha Island in the South China Sea. The
849 experiment was motivated by the need to understand ocean variability and how it
850 interacts with large (15 m) sand dunes on the sea floor. The dominant signal
851 observed consisted of sets of large amplitude nonlinear internal waves (NLIWs)
852 impinging on the continental slope from the southeast. These were in fact the very
853 same waves that impact the Dongsha Island region and have been reported by many
854 previous authors. The "sand dunes" waves however were about 50% smaller and
855 less energetic than the "Dongsha" waves, since the location was near the northern
856 extremity of the wave crests rather than near the main axis of the waves. The mean
857 bottom slope along the sand dunes mooring line was also gentler than farther
858 southwest. While the internal tides are no doubt important to the dune-building
859 process, this paper focuses entirely on the NLIW properties, most especially how the
860 waves were transformed as they shoaled up a very gradual bottom slope.   New
861 information gleaned includes the packet formation process, further insights on the
862 difference between a-waves and b-waves, and the energy transformation processes
863 which took place during wave shoaling.
864
865 During the fortnight observed, the a-waves began arriving several days ahead of the
866 b-waves and traveled in a more northerly direction. Once they started arriving, the
867 b-wave always lead the a-wave by 6-8 hours. In any given pair, the a-wave was
868 generally larger, but b-waves generated near spring tide may be larger than a-waves
869 generated near neap. The a-waves generally arrived at the site as 2-3 wave packets,
870 but the b-waves may also form packets as they shoal. The wave generation location
871 and their positioning relative to each other and the internal tide determines the
872 wave classification. The b-waves were located near the head of the upslope internal
873 tide while the a-waves developed more towards the back. The wave arrival patterns
874 rigorously tracked the tidal structure in Luzon Strait, even to the point of shifting by
875 six hours when the strong beat/weak beat pattern reversed in the strait during neap
876 tide. The arrival patterns were consistent with earlier work showing that the a-
877 waves were generated in the southern portion of the Luzon Strait and the b-waves
878 in the north.
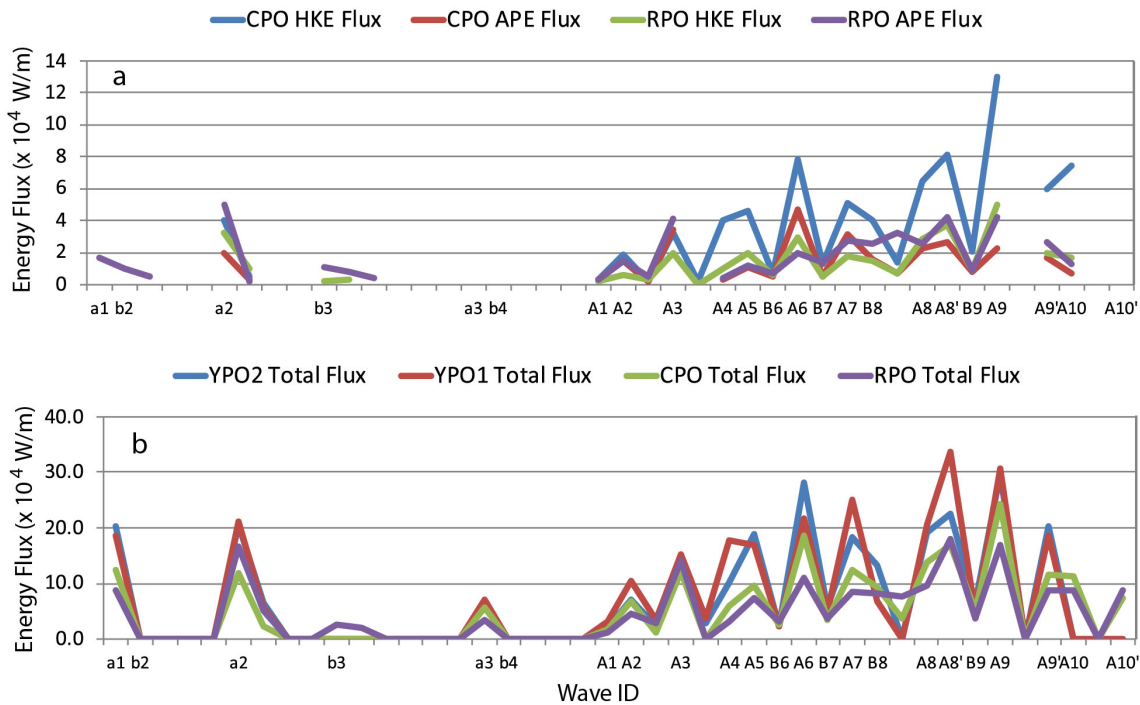
879
880
881 *Figure 16. The energy fluxes up the slope for each of the nonlinear internal waves*
882 *identified in the sand dunes moored array data. a) The kinetic and potential energy*
883 *flux for moorings CPO and RPO. b) The total energy flux for all four moorings. This is*
884 *the sum of the kinetic, potential, and pressure work terms.*

885

886 A conundrum remains the arrival of two large a-waves with nearly equal amplitude
887 separated by two hours during the period of maximal tidal forcing, spring tide plus
888 or minus one day. Additional work is needed to understand the origin of these
889 waves.

890

891 At least two packet-generating mechanisms were clearly observed. Most a-waves
892 had already formed in the deep basin by the time they were incident upon the most
893 offshore mooring, YPO2 at the 388 m isobath. The behavior of these waves
894 depended on their amplitude: waves smaller than about 50 m and 100 MJ m^{-1}
895 propagated adiabatically upslope with little change of form. Waves larger/more
896 energetic than this formed packets via wave dispersion. Wave breaking was not
897 observed at any time, with the possible exception of the largest wave that was
898 steepening on the backside at the shallowest mooring, RPO at 266 m depth. The
899 waves likely break, and/or reflect, inshore of 266 m where the bottom is also
900 steeper. On the other hand, some of the b-waves were incident on YPO2 while
901 others were absent at YPO2 and formed while the internal tide shoaled between
902 YPO2 and RPO. These waves and wave packets were formed by the breaking of the
903 leading, strongly convergent edge of the upslope-propagating internal tide (not to
904 be confused with a breaking NLIW). This process took place near mooring CPO on

905 the 342 m isobath.   This process occurred just once per day and was most easily
906 discerned by the downslope tidal current near the bottom which was not
907 complicated by upper ocean processes.
908
909 The energy transformations also depended on wave amplitude. For the smaller
910 waves (E < 100 MJ m^{-1}), the incident APE was greater than the HKE and continued to
911 grow upslope. For the larger waves, the incident HKE was larger than the APE, but
912 the flux of HKE decreased sharply upslope especially between 342m to 266 m, while
913 the flux of APE in that depth range increased slightly, resulting in greater APE than
914 HKE farther onshore. These results are in rough agreement with recent theory and
915 numerical simulations of shoaling waves.
916
917 With the possible exception of one (largest) wave, no breaking NLIWs were
918 observed anywhere in the moored array. This is because neither of the criteria for
919 breaking waves was met: The orbital velocities never exceeded the propagation
920 speed, and wave amplitudes were too small. This situation contrasts with a similar
921 depth range farther southwest, where larger waves were already actively breaking
922 at the 300 m isobath. The more periodic, less turbulent environment presented to
923 the subaqueous sand dune field may be relevant to its formation location along the
924 slope. This and other forcing factors will be taken up in more detail in a subsequent
925 work.
926
927
928

929 **Acknowledgements**
930
931 This work was supported by the U.S. Office of Naval Research (ONR) under grant
932 N000141512464 and by the Taiwan Ministry of Science and Technology (MOST).
933 Wen-Hwa Her (IONTU) and Marla Stone (NPS) led the mooring work at sea. We
934 thank the officers and crew of the research vessels OCEAN RESEARCHER 1, OCEAN
935 RESEARCHER 3, and OCEAN RESEARCHER 5.
936
937
938

References

Alford, M. H., Lien, R.-C., Simmons, H., Klymak, J., Ramp, S. R., Yang, Y.-J., Tang, T.-Y., Farmer, D., and Chang, M.-H.: Speed and evolution of nonlinear internal waves transiting the South China Sea, J. Phys. Oceanogr., 40, 1338-1355, 2010.

Alford, M. H., MacKinnon, J. A., Nash, J. D., Simmons, H., Pickering, A., Klymak, J. M., Pinkel, R., Sun, O., Rainville, L., Musgrave, R., Beitzel, T., Fu, K.-H., and Lu, C.-W.: Energy flux and Dissipation in Luzon Strait: Two tales of two ridges, J. Phys. Oceanogr. 41, 2211-2222, 2011.

Alford, M. H., Peacock, T., and co-authors: The formation and fate of internal waves in the South China Sea, Nature, 521, 65-69, 2015.

Buijsman, M. C., Kanarska, Y., and McWilliams, J. C.: On the generation and evolution of nonlinear internal waves in the South China Sea, J. Geophys. Res.-Oceans, 115, C02012, doi:10.1029/2009JC005275, 2010a.

Buijsman, M. C., McWilliams, J. C., and Jackson, C. R.: East-west asymmetry in nonlinear internal waves from Luzon Strait, J. Geophys. Res.-Oceans, 115, C1057, doi:10.1029/2009JC006004, 2010b.

Chang, M.-H., Lien, R.-C., Tang, T. Y., D'Asaro, E. A., and Yang, Y. J.: Energy flux on nonlinear internal waves in the northern South China Sea, Geophys. Res. Let., 33, L03607, doi:10.1029/2005GL025196, 2006.

Chang, M.-H., Lien, R.-C., Lamb, K. G., and Diamessis, P. J.: Long-term observations of shoaling internal solitary waves in the northern South China Sea, J. Geophys. Res.-Oceans, 126, https://doi.org/10.1029/2020JC017129, 2021a.

Chang, M.-H., Cheng, Y.-H., Yang, Y.-J., Jan, S., Ramp, S. R., Reeder, D. B., Hseih, W.-T., Ko, D. S., Davis, K. A., Shao, H.-J., and Tseng, R.-S.: Direct measurements reveal instabilities and turbulence within large amplitude internal solitary waves beneath the ocean, Communications Earth & Environments, 2, doi:10.1038/S43247-020-00083-6, 2021b.

Chen, Y.-J., Ko, D. S., and Shaw, P.-T.: The generation and propagation of internal solitary waves in the South China Sea, J. Geophys. Res.-Oceans, 118, 6578-6589, doi:10.1002/2013JC009319, 2013.

979 Chiu, L. Y. S., and Reeder, D. B.: Acoustic mode coupling due to subaqueous sand
980 dunes in the South China Sea, J. Acoust. Soc. Am., 134, doi:10.1121/1.4812862, 2013.
981
982 Chiu, L. Y. S., Chang, A. Y. Y., and Reeder, D. B.: Resonant interaction of acoustic
983 waves with subaqueous bedforms: Sand dunes in the South China Sea, J. Acoust. Soc.
984 Am., 138, doi:10.1121/1.4937746, 2015.
985
986 Du, T., Tseng, Y.-H., and Yan, X.-H.: Impacts of tidal currents and Kuroshio intrusion
987 on the generation of nonlinear internal waves in Luzon Strait, J. Geophys. Res.-
988 Oceans, 113, C08015, doi:10.1029/2007JC004294, 2008.
989
990 Duda, T. F., Lynch, J. F., Irish, J. D., Beardsley, R. C., Ramp, S. R., Chiu, C.-S., Tang,
991 T.-Y., and Yang, Y.-J.: Internal tide and nonlinear internal wave behavior at the
992 continental slope in the northern South China Sea, IEEE/J. Oc. Eng., 29, 1105-
993 1131, 2004.
994
995 Egbert, G., and Erofeeva, S.: Efficient inverse modeling of barotropic ocean tides,
996 J. Atmos. Oceanic Technol., 19, 183-204, 2002.
997
998 Farmer, D., Li, Q., and Park, J.-H.: Internal wave observations in the South China Sea:
999 The role of rotation and non-linearity, Atmosphere-Ocean, 47, 267-280, 2009.
1000
1001 Farmer, D. M., Alford, M. H., Lien, R.-C., Yang, Y. J., Chang, M.-H., and Li, Q.: From
1002 Luzon Strait to Dongsha Plateau: Stages in the life of an internal wave,
1003 Oceanography, 24, 64-77, 2011.
1004
1005 Grimshaw, R., Pelinovsky, E. N., Talipova, T. G., and Kurkina, A.: Simulations of the
1006 transformation of internal solitary wave on oceanic shelves, J. Phys. Oceanogr., 34,
1007 2774-2791, 2004.
1008
1009 Grimshaw, R., Guo, C., Helfrich, K., and Vlasenko, V.: Combined effect of rotation and
1010 topography on shoaling oceanic internal solitary waves, J. Phys. Oceanogr., 44, 1116-
1011 1132, 2014.
1012
1013 Helfrich, K. R., and Melville, W. K.: On long nonlinear internal waves over slowly
1014 varying topography, J. Fluid Mech., 149, 305-317, 1986.
1015
1016 Helfrich, K. R.: Internal solitary wave breaking and run-up on a uniform slope, J.
1017 Fluid Mech., 243, 133-154, 1992.
1018
1019 Jackson, C. B.: An empirical model for estimating the geographic location of
1020 nonlinear internal solitary waves, J. Atmos. Oceanic Technol., 26, 2243-2255, 2009.
1021
1022
1023

1024 Klymak, J. M., Pinkel, R., Liu, C.-T., Liu, A. K., and David, L.: Prototypical solitons in
1025 the South China Sea, Geophys. Res. Lett., 33, L11607,
1026 doi:10.1029/2006GL025932, 2006.
1027
1028 Kunze, E., Rosenfeld, L. K., Carter, G. S, and Gregg, M. C.: Internal waves in
1029 Monterey Submarine Canyon, J. Phys. Oceanogr., 32, 1890-1913, 2002.
1030
1031 Helfrich, K. R., Trowbridge, J. H., and Reeder, D. B.: High dissipation of an internal
1032 solitary wave over sand dunes, J. Phys. Oceanogr., in review.
1033
1034 Hsu, M.-K., and Liu, A. K.: Nonlinear internal waves in the South China Sea, Canadian
1035 Journal of Remote Sensing 26, 72-81, 2000.
1036
1037 Lamb, K. G.: A numerical investigation of solitary internal waves with trapped
1038 cores formed via shoaling, J. Fluid Mech., 451, 109-144, 2002.
1039
1040 Lamb, K. G., and Nguyen, V. T.: Calculating energy flux in internal solitary waves with
1041 an application to reflectance, J. Phys. Oceanogr., 39, 559-580, 2009.
1042
1043 Lamb, K. G., and Warn-Varnas, A.: Two-dimensional numerical simulations of
1044 shoaling internal solitary waves at the ASIAEX site in the South China Sea, Nonlin.
1045 Processes Geophys., 22, 289-312, 2015.
1046
1047 Lee, C. M, Kunze, E., Sanford, T. B., Nash, J. D., Merrifield, M. A., and Holloway, P.
1048 E.: Internal tides and turbulence along the 3000-m isobath of the Hawaiian
1049 Ridge, J. Phys. Oceanogr., 36, 1165-1183, 2006.
1050
1051 Li, Q., and Farmer, D. M.: The generation and evolution of nonlinear internal
1052 waves in the deep basin of the South China Sea, J. Phys. Oceanogr., 41, 1345-
1053 1363, 2011.
1054
1055 Lien, R. C., D'Asaro, E. A., Henyey, F., Chang, M. H., Tang, T. Y. and Yang, Y-J.:
1056 Trapped core formation within a shoaling nonlinear internal wave, J. Phys.
1057 Oceanogr., 42, 511-525 2012.
1058
1059 Lien, R. C., Henyey, F., Ma, B., and Yang, Y. J.: Large-amplitude internal solitary
1060 waves observed in the northern South China Sea: Properties and Energetics, J.
1061 Phys. Oceanogr., 44, 1095-1115, 2014.
1062
1063 Liu, A. K., Ramp, S. R., Zhao, Y., and Tang, T. Y.: A case study of internal solitary wave
1064 propagation during ASIAEX 2001, IEEE/J. Oc. Eng., 29, 1144-1156, 2004.
1065
1066

1067   Moum, J. N., Klymak, J. M., Nash, J. D., Perlin, A., and Smyth, W. D.: Energy
1068   transport by nonlinear internal waves, J. Phys. Oceanogr., 37, 1968-1988, 2007.
1069
1070   Nash, J. D., Alford, M. H., and Kunze, E.: Estimating internal wave energy fluxes in the
1071   ocean, J. Atm. and Oc. Tech., 22, 1551-1570, 2005.
1072
1073   Nash, J. D., Kunze, E., Lee, C. M., and Sanford, T. B.: Structure of the baroclinic tide
1074   generated at Kaena Ridge, Hawaii, J. Phys. Oceanogr., 36, 1123-1135, 2006.
1075
1076   Nash, J. D., Kelly, S. M., Shroyer, E. L., Moum, J. N., and Duda, T. F.: The unpredictable
1077   nature of internal tides on the continental shelf, J. Phys. Oceanogr., 42, 1981-2000,
1078   2012.
1079
1080   Orr, M. H., Mignerey, P. C.: Nonlinear internal waves in the South China Sea:
1081   Observations of the conversion of depression internal waves to elevation internal
1082   wages, J. Geophys. Res. 108, 3064, doi:10.1029/2001JC001163, 2003.
1083
1084   Ramp, S.R., Chiu, C. S., Kim, H.-R., Bahr, F. L., Tang, T.-Y., Yang, Y. J., Duda, T., and
1085   Liu, A. K.: Solitons in the Northeastern South China Sea Part I: Sources and
1086   Propagation Through Deep Water, IEEE/J. Oc. Eng., 29, 1157-1181, 2004.
1087
1088   Ramp, S. R., Yang, Y. J., and Bahr, F. L.: Characterizing the nonlinear internal wave
1089   climate in the northeastern South China Sea, Nonlin. Processes Geophys., 17, 481-
1090   498, doi:10.5194/npg-17-481-2010, 2010.
1091
1092   Ramp, S. R., Park, J.-H., Yang, Y. J., Bahr, F. L., and Jeon, C.: Latitudinal Structure of
1093   Solitons in the South China Sea, J. Phys. Oceanogr., 49, 1747-1767, 2019.
1094
1095   Ramp, S. R., Yang, Y.-J., Jan, S., Chang, M.-H., Davis, K. A., Sinnett, G., Bahr, F. L.,
1096   Reeder, D. B., Ko, D. S., and Pawlak, G.: Solitary waves impinging on an isolated
1097   tropical reef: Arrival patterns and wave transformation under shoaling, J. Geophys. Res.-
1098   Oceans, in review.
1099
1100   Reeder, D. B., Ma, B., and Yang, Y. J.: Very large subaqueous sand dunes on the upper
1101   continental slope in the South China Sea generated by episodic, shoaling deep-water
1102   internal solitary waves, Mar. Geol., 279, 12-18, 2011.
1103
1104   Rivera-Rosario, G., Diamessis, P. J., Lien, R.-C., Lamb, K. G., & Thomsen, G. N.:
1105   Formation of recirculating cores in convectively breaking internal solitary waves of
1106   depression shoaling over gentle slopes in the South China Sea, J. Phys. Oceanogr., 50,
1107   1137–1157, https://doi.org/10.1175/jpo-d-19-0036.1, 2020
1108

1109   Scotti, A., Beardsley, R. C., and Butman, B.: On the interpretation of energy and
1110   energy fluxes of nonlinear internal waves: An example from Massachusetts Bay, J.
1111   Fluid Mech., 561, 103-112, 2006.

1112

1113   Small, J.: A nonlinear model of the shoaling and refraction of interfacial solitary
1114   waves in the ocean. Part I: Development of the model and investigations of the
1115   shoaling effect, J. Phys. Oceanogr., 31, 3163-3183, 2001.

1116

1117   Small, J.: A nonlinear model of the shoaling and refraction of interfacial solitary
1118   waves in the ocean. Part II: Oblique refraction across a continental slope and
1119   propagation over a seamount, J. Phys. Oceanogr., 31, 3184-3199, 2001.

1120

1121   Turkington, B., Eydeland, A., and Wang, S.: A computatioinal method for solitary
1122   internal waves in a continuously stratified fluid, Stud. Appl. Maths., 85, 93-127,
1123   1991.

1124

1125   Vlasenko, V., Ostrovsky, V. L., and Hutter, K.: Adiabatic behavior of strongly
1126   nonlinear internal solitary waves in slope-shelf areas, J. Geophys. Res., 110, C04006,
1127   doi:10.1029/2004JC002705, 2005.

1128

1129   Vlasenko, V., Guo, C., and Stashchuk, N.: On the mechanism of A-type and B-type
1130   internal solitary wave generation in the northern South China Sea, Deep-Sea Res. I,
1131   69, 100-112, 2012.

1132

1133   Vlasenko, V., and Stashchuk, N.: Three-dimensional shoaling of large-amplitude
1134   internal waves, J. Geophys. Res.-Oceans, 112, C11018, doi:10.1029/2007JC004107,
1135   2007.

1136

1137   Vlasenko, V., and Hutter, K.: Numerical experiments on the breaking of solitary
1138   internal waves over a slope-shelf topography, J. Phys. Oceanogr., 32, 1779-1793,
1139   2002.

1140

1141   Yang, Y. J., Fang, Y. C., Chang, M.-H., Ramp, S. R., Kao, C.-C., and Tang, T.-Y.:
1142   Observations of second baroclinic mode internal solitary waves on the continental
1143   slope of the northern South China Sea, J. Geophys. Res.-Oceans, 114, C10003,
1144   doi:10.1029/2009JC005318, 2009.

1145

1146   Yang, Y. J., Fang, Y. C., Chang, Y.-T., Tang, T. Y., and Ramp, S. R.: Convex and concave
1147   types of second baroclinic mode internal solitary waves, Nonlin. Processes
1148   Geophys., 17, 605-614, doi:10.5194/npg-17-605-2010, 2010.

1149

1150   Zhang, Z., Fringer, O. B., and Ramp, S. R.: Three-dimensional, nonhydrostatic
1151   numerical simulation of nonlinear internal wave generation and propagation in the
1152   South China Sea, J. Geophys. Res.-Oceans, 116, C05022, doi:10.1029/2010JC006424,
1153   2011.

1154

1155 **APPENDIX A**

1156

Table 1. Mooring and Instrument Locations and Performance									
Mooring	Latitude (north)	Longitude (east)	Bottom Depth (m)	Instrument	Instrument Depth (m)	Start	Stop	Record Length (d)	Sample Interval (s)	Number of Points
RPO	21 53.334	117 33.676	266			6/1/14	6/18/14	18		
				★ADCP 300 kHz	31				90	17198
				★ADCP 300 kHz	105				90	17197
				★ADCP 300 kHz	190				90	17198
				SBE 37 (TSP)	27, 105, 184, 244				20	76354
				SBE 39 (TP)	61, 91, 141, 170, 258				10	154792
				SPE 56 (T)	45, 75, 125, 155, 199, 229				10	154794
CPO	21 51.879	117 36.587	342			6/1/14	6/18/14	18		
				★ADCP 300 kHz	11				90	16394
				◆ADCP 300 kHz	263				90	16398
				★ADCP 300 kHz	269				90	16410
				SBE 37 (TSP)	43, 109, 169, 230, 307				10	148066
				SBE 39 (TP)	78, 139, 200, 286				10	148066
YPO1	21 49.998	117 37.600	372			6/2/14	6/19/14	18		
				✚ADCP 75 kHz	20				90	16537
				★ADCP 300 kHz	306				90	16537
				SBE 19 (TSP)	369		6/13/14	12	15	63517
				SBE 39 (TP)	35, 56, 92, 117, 178, 240				10	148845
				SBE 39 (TP)	300		6/17/14	16	10	134727
				SBE 39 (TP)	354		6/10/14	9	10	70620
				SBE 56 (T)	76		6/8/14	7	10	54078
				SBE 56 (T)	147, 209, 270, 325				10	148845
				Star Oddi (TP)	148, 188		6/11/14	10	10	77398
YPO2	21 48.679	117 39.512	386			6/2/14	6/19/14	18		
				✚ADCP 75 kHz	20				90	16916
				★ADCP 300 kHz	301				90	16915
				SBE 39 (TP)	58, 97, 118, 180, 241				10	152252
				SBE 39 (TP)	37, 354		6/17/14		10	133147
				SBE 56 (T)	78, 149, 201, 272, 328				10	152252
Source	21 52.630	117 37.128	328			6/1/14	6/18/14	18		
				SBE 37 (TSP)	26, 86, 147, 208, 268				10	142186
				SBE 39 (TP)	55, 116, 174, 238, 310				10	1142186
★4-m bins down-looking, 30 pings per ensemble										
◆4-m bins up-looking, 30 pings per ensemble										
✚16-m bins down-looking, 10 pings per ensemble										

1157